RSC Advances

PAPER

View Article Online
View Journal | View Issue

Cite this: *RSC Adv.*, 2025, **15**, 50910

First-principles study of vanadium-based Half-Heusler compounds: structural, electronic, optical, and thermomechanical properties for optoelectronics

Md. Tarekuzzaman,[a] Salah Uddin,[a] Md. Shahazan Parves,[a] Fahad Alhashmi Alamer,[b] Omar Alsalmi[b] and Md. Zahid Hasan *[a]

This research explores the physical properties of Half-Heusler compounds, specifically VFeAs, VFeBi, VIrPb, and VIrSn, utilizing Density Functional Theory (DFT) through the Cambridge Serial Total Energy Package (CASTEP). The study begins with structural optimization, which confirms that these compounds maintain stability within cubic crystal structures. A comprehensive analysis of their electronic band structures and density of states (DOS) reveals band gaps of 1.615 eV for VFeAs, 1.378 eV for VFeBi, 1.361 eV for VIrPb, and 1.574 eV for VIrSn, indicating that these materials exhibit semiconductor properties. To assess mechanical stability and ductility, the research evaluates the elastic constants of these compounds, which meet the Born stability criteria. The analysis of elastic moduli further indicates that VFeAs, VFeBi, VIrPb, and VIrSn demonstrate elastic isotropy. The study also analyzes key optical properties, such as the absorption coefficient, dielectric function, electrical conductivity, reflectivity, refractive index, and loss function. The findings highlight significant photoconductive behavior, high optical reflectivity, and favorable dielectric properties, suggesting that these materials hold considerable promise for use in optoelectronic devices. Moreover, the compounds exhibit low minimum thermal conductivity (K_{min}) and a reduced Debye temperature (θ_D), making them promising candidates for thermal barrier coating (TBC) applications in cutting-edge thermal management technologies.

Received 15th November 2025
Accepted 8th December 2025

DOI: 10.1039/d5ra08828c

rsc.li/rsc-advances

1. Introduction

Heusler compounds, first discovered in 1903, have since become a basis of materials science due to their unique electronic, magnetic, and thermoelectric properties. These intermetallic alloys are generally classified into two categories based on their stoichiometry: full Heusler (2 : 1 : 1) and Half-Heusler (1 : 1 : 1) compounds. Over 1500 Heusler compounds have been identified, and they have been thoroughly studied for various applications, including semiconductors, superconductors, magnetic materials, and thermoelectrics.[1,2] The rich diversity in their atomic structures and compositions enables a wide range of properties, making them ideal for a variety of technological advancements, from energy conversion to quantum computing.[3,4] Among the different types of Heusler compounds, Half-Heusler (HH) alloys are particularly noteworthy for their exceptional tunability in terms of electronic, magnetic, and thermal properties. The general formula for HH compounds is XYZ, and they crystallize in a cubic MgAgAs-type structure under space group $F\bar{4}3m$ (no. 216). Their adaptable properties are governed by the careful manipulation of composition, doping, and structural modifications. These materials are characterized by their robust mechanical strength, high thermal stability, and favorable electronic structures, making them ideal for applications in thermoelectric, optoelectronics, spintronics, and catalysis.[5,6] The semiconducting behavior of HH alloys can be precisely tailored by altering the atomic constituents. These materials exhibit a wide range of band gaps, ranging from 0 to 4 eV, which can be adjusted through the use of electron or hole doping, as well as by changing the electronegativity of constituent elements.[7,8] The ability to control the electronic structure in this way makes these compounds promising candidates for next-generation semiconductor technologies. Furthermore, doping with rare-earth elements or transition metals, such as manganese, can introduce magnetism, opening up new possibilities for spintronic applications.[9,10] As a result, HH alloys are at the forefront of materials research, with their potential use in energy-efficient technologies, quantum computing, and advanced electronics.

One of the most significant advantages of HH compounds is their performance in thermoelectric applications.

[a]*Materials Research and Simulation Lab, Department of Electrical and Electronic Engineering, International Islamic University Chittagong, Kumira, Chittagong, 4318, Bangladesh. E-mail: zahidhasan.02@gmail.com*

[b]*Department of Physics, College of Science, Umm Al-Qura University, Makkah 21955, Saudi Arabia*

Thermoelectric materials convert waste heat into electricity, providing a sustainable method for energy recovery. As such, these materials have become crucial for applications in energy harvesting, refrigeration, and waste heat recovery.[11] In addition to their thermoelectric properties, HH alloys have found extensive use in spintronics, where electron spin is utilized to enhance the functionality of electronic devices. Spintronic materials can exploit the intrinsic angular momentum of electrons to enable faster and more energy-efficient data storage and transmission. HH compounds such as CoMnSb and NiMnSb exhibit nearly 100% spin polarization, making them ideal candidates for use in spin valves, magnetic tunnel junctions, and other spintronic devices.[12,13] These materials offer substantial advantages in terms of energy efficiency and data storage density, paving the way for next-generation memory and logic devices. HH compounds are also valuable for optoelectronic applications, including light-emitting diodes (LEDs) and solar cells. Their tunable electronic structure allows for the optimization of optical absorption and emission, making them ideal candidates for energy-efficient lighting and photovoltaic devices.[14] While traditional semiconductors like CdS have been widely used in photovoltaics, their environmental impact has driven research toward more sustainable alternatives with optimized band gaps and band alignments.[15] In particular, materials such as RhTiP, RhTiAs, and RhTiSb exhibit significant optical absorption in both the visible and ultraviolet spectra, positioning them as strong candidates for next-generation photovoltaic technologies.[16,17] Furthermore, these materials' high optical absorption and well-aligned band gaps enhance the efficiency of solar cells, especially when used in combination with appropriate buffer layers.[18] In addition, the discovery of lithium-based ternary semiconductors, such as LiAlGe, LiAlSi, and LiGaSi, highlights the growing potential of HH compounds in optoelectronic and photovoltaic applications.[19] The mechanical stability of Half-Heusler (HH) compounds has been studied in terms of structural integrity, elasticity, and deformation. ZrNiSn and TiNiSn exhibit high mechanical strength due to their ordered crystal structures.[20] NbFeSb shows robust fracture toughness and compressive strength, particularly under high-temperature conditions.[21] In the realm of topological materials, certain HH compounds have been predicted to behave as topological insulators, thanks to strong spin–orbit coupling effects. These materials allow for surface conduction while maintaining bulk insulation, which is essential for developing low-energy electronics and quantum computing devices.[22,23] The discovery of materials like LuPtBi, which exhibits superconductivity below 1 K, further emphasizes the potential of HH alloys in quantum technologies.[24] The pursuit of topological superconductors is a key area of research for the development of quantum computing and other advanced technologies that rely on the manipulation of quantum states.[25]

In this work, we investigate the structural, electronic, mechanical, elastic anisotropy and thermodynamic properties of four specific Half-Heusler compounds: VFeAs, VFeBi, VIrPb, and VIrSn. These compounds were selected due to their promising semiconducting nature and potential applications in optoelectronics, and photovoltaics. The band gaps of these compounds align with their suitability for energy conversion, making them prime candidates for the development of advanced electronic devices. By comparing these materials with previously studied HH compounds, this research provides valuable insights into their properties and applications, further advancing our understanding of HH alloys and their role in future technological innovations. The findings from this work are expected to stimulate both theoretical and experimental studies, contributing to the development of sustainable energy solutions and next-generation electronics.

2. Computational method

The structural, electronic, elastic, and optical properties of the vanadium-based Half-Heusler compounds VFeAs, VFeBi, VIrPb, and VIrSn were systematically investigated using first-principles calculations based on density functional theory (DFT), as implemented in the CASTEP (Cambridge Serial Total Energy Package) code.[26] CASTEP employs a plane-wave pseudopotential approach within DFT, and in this study, the exchange–correlation effects were treated using the generalized gradient approximation (GGA) in the Perdew–Burke–Ernzerhof (PBE) formulation,[27] which is well known for balancing accuracy with computational efficiency. The valence electron configurations used for the constituent elements were: V ($3d^3\ 4s^2$), Fe ($3d^6\ 4s^2$), As ($4s^2\ 4p^3$), Bi ($6s^2\ 6p^3$), Ir ($5d^7\ 6s^2$), Pb ($6s^2\ 6p^2$), and Sn ($5s^2\ 5p^2$). A plane-wave cutoff energy of 800 eV was selected to ensure the convergence of total energy and structural parameters, while the Brillouin zone integrations were performed using a Monkhorst–Pack k-point mesh of $8 \times 8 \times 8$. Geometry optimization was achieved using the Broyden–Fletcher–Goldfarb–Shanno (BFGS) minimization algorithm,[28] with convergence thresholds set as follows: 5.0×10^{-6} eV per atom for energy, 0.01 eV $Å^{-1}$ for maximum force, 5.0×10^{-4} Å for atomic displacement, and 0.02 GPa for stress. The elastic constants (C_{ij}) were computed *via* the stress–strain method,[29] using stricter convergence parameters: energy tolerance of 1.0×10^{-6} eV per atom, force tolerance of 0.02 eV $Å^{-1}$, and displacement tolerance of 4.0×10^{-4} Å. Mechanical anisotropy was further explored using ELATE (Elastic Tensor Analysis),[30] which generated both 2D and 3D visualizations of Young's modulus, shear modulus, and Poisson's ratio, highlighting the directional dependence of mechanical behavior. The electronic structure, including band structure and density of states (DOS), was initially calculated using the GGA-PBE functional, while the Heyd–Scuseria–Ernzerhof (HSE06) hybrid functional was subsequently employed to obtain more accurate electronic parameters such as the band gap and band edge alignments.[31] Finally, the optical properties were derived from the mathematical formulations of the dielectric function, absorption coefficient, reflectivity, refractive index, and other related quantities provided in the respective section, where all physical symbols retain their conventional meanings.[32,33] The complex dielectric function, expressed in terms of its real part $\varepsilon_1(\omega)$ and imaginary part $\varepsilon_2(\omega)$, provides the fundamental framework for evaluating various optical properties, including the absorption

coefficient $\alpha(\omega)$, refractive index $n(\omega)$, reflectivity $R(\omega)$, and energy loss function $L(\omega)$. These properties are derived from the frequency-dependent dielectric response and are defined as follows:

(1) Real part of the dielectric function:

$$\varepsilon_1(\omega) = \frac{2}{\pi} P \int_0^{\infty} \frac{\omega' \varepsilon_2(\omega')}{\omega'^2 - \omega^2} \mathrm{d}\omega' + 1 \quad (1)$$

where P denotes the principal value of the integral, ω' is the photon frequency, and $\varepsilon_2(\omega')$ is the imaginary part of the dielectric function.

(2) Imaginary part of the dielectric function:

$$\varepsilon_2(\omega) = \frac{2\pi e^2}{\Omega \varepsilon_0} \sum_{k,v,c} \left| \langle \Psi_k^c | \hat{u} \cdot \vec{r} | \Psi_k^v \rangle \right|^2 \delta\left(E_k^c - E_k^v - E\right) \quad (2)$$

where e is the elementary charge, Ω is the unit cell volume, ε_0 is the vacuum permittivity, Ψ_k^v and Ψ_k^c are the valence and conduction band wave functions at wave vector k, u is the polarization vector of the incident electric field, and δ is the Dirac delta function ensuring energy conservation.

(3) Absorption coefficient:

$$\alpha(\omega) = \sqrt{2\omega \left[\sqrt{\varepsilon_1^2(\omega) + \varepsilon_1^2(\omega)} - \varepsilon_1(\omega) \right]^{\frac{1}{2}}} \quad (3)$$

It represents the rate at which light is absorbed per unit distance.

(4) Refractive index:

$$n(\omega) = \left[\frac{\varepsilon_1(\omega) + \omega_2^2(\omega)^{\frac{1}{2}}}{2} + \frac{\varepsilon_1(\omega)}{2} \right]^{\frac{1}{2}} \quad (4)$$

It described the phase velocity of light in the medium.

(5) Reflectivity:

$$R(\omega) = \left[\frac{\left(\varepsilon(\omega)^{\frac{1}{2}} - 1 \right)}{\left(\varepsilon(\omega)^{\frac{1}{2}} - 1 \right)} \right]^2 \quad (5)$$

which gives the fraction of incident light reflected at the surface.

(6) Energy loss function:

$$L(\omega) = \frac{\varepsilon_2(\omega)}{\varepsilon_1^2(\omega) + \varepsilon_2^2(\omega)} \quad (6)$$

It indicated the energy loss of a fast electron traversing the material.

3. Results and discussion

3.1 Structural properties

The VXY series of compounds, where X represents Fe or Ir and Y represents As, Bi, Pb, or Sn, are categorized as Half-Heusler materials. These compounds crystallize in the $F\bar{4}3m$ space group (no. 216), a characteristic shared with other MgAgAs-type crystal structures.[34,35] A single formula unit (XYZ) has 3 atoms in the primitive cell. The Conventional crystal structures of VXY (X = Fe, Ir and Y = As, Bi, Pb, Sn) is depicted in Fig. 1. Our optimized lattice constants 5.46 Å (VFeAs), 5.88 Å (VFeBi), 6.19 Å (VIrPb), and 6.08 Å (VIrSn) show deviations within ≤0.8% from reported values, demonstrating high consistency and confirming the reliability of our structural predictions (see Table 1). The systematic progression observed in these optimized lattice parameters underscores the reliability of the Density Functional Theory (DFT) methodology employed in this research, affirming its capacity for predicting the structural characteristics of the Half-Heusler framework. This consistent behavior also suggests that the atomic arrangement within these compounds remains structurally robust across the various compositions. Optimal structural stability in these VXY Half-Heusler alloys is achieved when the atoms occupy specific Wyckoff positions: V atoms at 4a (0, 0, 0), Fe or Ir atoms at 4b (0, 0, 0.5), and As, Bi, Pb, or Sn atoms at 4c (0.75, 0.25, 0.75). Further theoretical data presented in Table 1 aligns well with our computational findings for the lattice parameters and unit cell volumes of the VXY compounds, thereby validating the accuracy of our current calculations.

The formation energy (ΔE_f) was calculated as:

$$\Delta E_f(\mathrm{VXY}) = [E_{\mathrm{tot.}}(\mathrm{VXY}) - E_s(\mathrm{V}) - E_s(\mathrm{X}) - E_s(\mathrm{Y})] \quad (7)$$

where $E_{\mathrm{tot.}}$ is the total energy of the unit cell, and E_s(V), E_s(X), and E_s(Y) are the energies of the constituent atoms in their standard states. All of Heusler compounds show the negative formation energies, indicating their thermodynamic stability.

The optimized nearest-neighbor bond lengths (Table 2) reveal clear and consistent trends across all studied compounds. In VFeAs and VFeBi, the Fe–As (2.37 Å) and Fe–Bi (2.55 Å) bonds are shorter than the corresponding V–As (2.74 Å) and V–Bi (2.95 Å) distances, indicating comparatively stronger bonding between Fe and the pnictogen atoms. A similar pattern appears in VIrPb and VIrSn, where the Ir–Pb (2.68 Å) and Ir–Sn (2.64 Å) bonds remain shorter than the associated V–Pb and V–Sn bonds (3.05–3.10 Å). These trends confirm that the transition-metal–anion interactions dominate the local bonding environment and demonstrate the structural consistency of the optimized geometries.

3.2 Electronic properties

To precisely evaluate key electronic properties such as the band structure and total density of states (TDOS), it is essential to have a thorough understanding of the electrical behavior of cubic materials, particularly ternary Heusler alloys like VXY (X = Fe, Ir and Y = As, Bi, Pb, Sn). The electronic band structure and the density of states are the two fundamental parameters that govern a material's electrical characteristics. These electronic features not only determine charge transport behavior but also provide critical insights into the material's optical properties and help classify it as a conductor, semiconductor, or insulator.[37] This investigation provides valuable understanding of the relationship between solid-state band structures and the

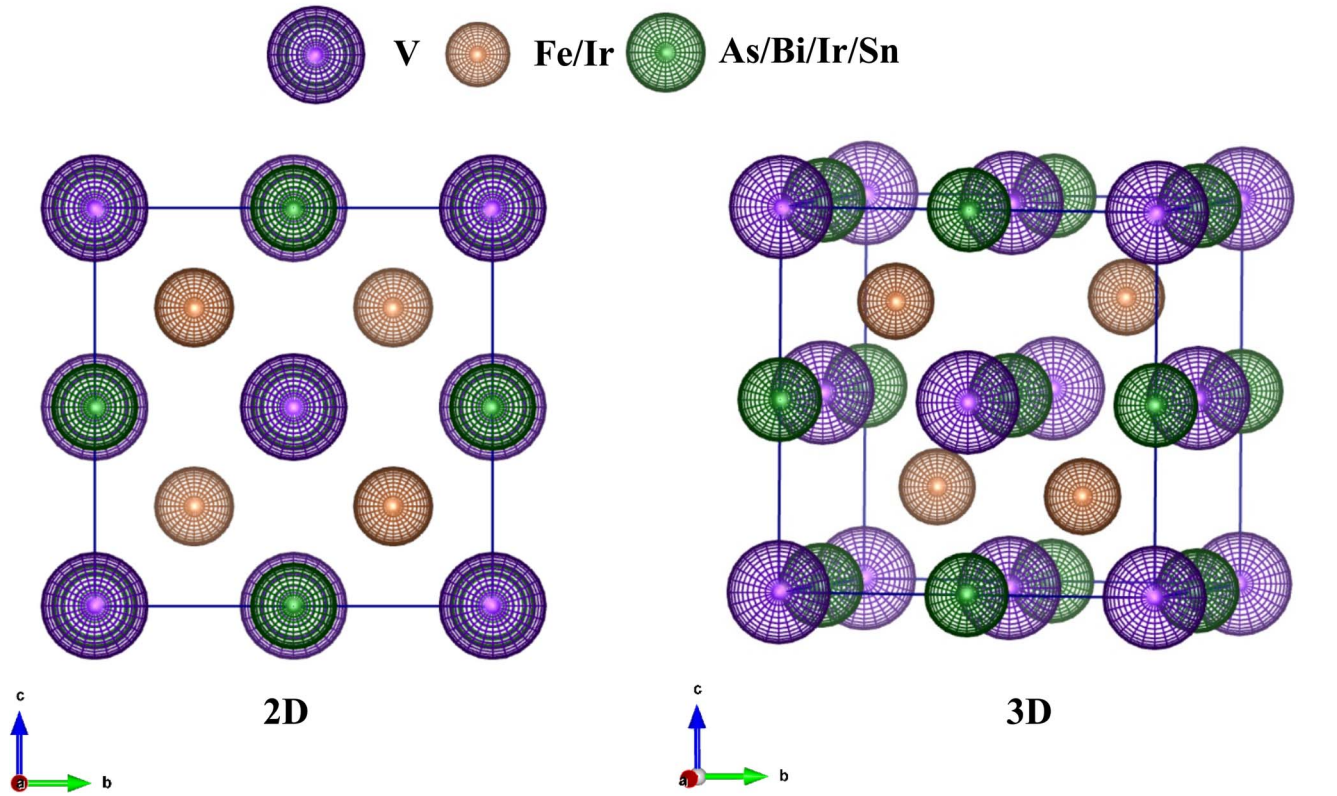

Fig. 1 Conventional crystal structures of VXY (X = Fe, Ir and Y = As, Bi, Pb, Sn).

corresponding crystal properties.[38,39] Following structural optimization, the electronic characteristics of VXY (X = Fe, Ir and Y = As, Bi, Pb, Sn) were analyzed using first-principles calculations within the framework of the HSE06 hybrid functional. The computed electronic band structures and total density of states (DOS) for the cubic phases are depicted in Fig. 2 and 4, along the high-symmetry path W–L–Γ–X–W–K. The Fermi level, positioned at 0 eV, is indicated by a dashed line and serves as the reference separating the valence and conduction bands. The electronic band structures are displayed within an energy range of −4 to +4 eV. All four materials VFeAs, VFeBi, VIrPb, and VIrSn exhibit semiconducting behavior characterized by indirect band gaps, where the valence band maximum (VBM) and conduction band minimum (CBM) occur at different *k*-points. The calculated band gap values are 1.615 eV for VFeAs, 1.378 eV for VFeBi, 1.361 eV for VIrPb, and 1.574 eV for VIrSn. Since experimental band-gap values for these specific compositions are not available. Therefore, we compared our HSE06 results with previous GGA-based calculations for related Half-Heusler compounds. As expected, the hybrid functional yields larger band gaps, confirming the consistency and reliability of our electronic results.

The influence of spin–orbit coupling (SOC) on the electronic structure of VFeAs, VFeBi, VIrPb, and VIrSn is presented in Fig. 3. The inclusion of SOC introduces noticeable band

Table 1 Optimized unit cell volumes V (Å^3) and lattice parameters $a = b = c$ (Å) and formation enthalpy ΔH_f (eV per atom) for VXY (X = Fe, Ir and Y = As, Bi, Pb, Sn)

Compounds	$a = b = c$ (Å)	V (Å^3)	ΔH_f (eV per atom)	Ref.
VFeAs	5.46	163.13	−0.469	This study
	5.49			36
VFeBi	5.88	203.31	−0.100	This study
	5.93			36
VIrPb	6.19	237.85	−0.349	This study
	6.19			36
VIrSn	6.08	225.22	−0.427	This study
	6.08			36

Table 2 Optimized nearest-neighbor bond distances (Å) for the VFeAs, VFeBi, VIrPb, and VIrSn Half-Heusler compounds

Compound	Bond type	Bond length (Å)
VFeAs	Fe–As	2.37
	V–Fe	2.37
	V–As	2.74
VFeBi	Fe–Bi	2.55
	V–Fe	2.55
	V–Bi	2.95
VIrPb	Ir–Pb	2.68
	V–Ir	2.68
	V–Pb	3.10
VIrSn	Sn–Ir	2.64
	V–Ir	2.64
	V–Sn	3.05

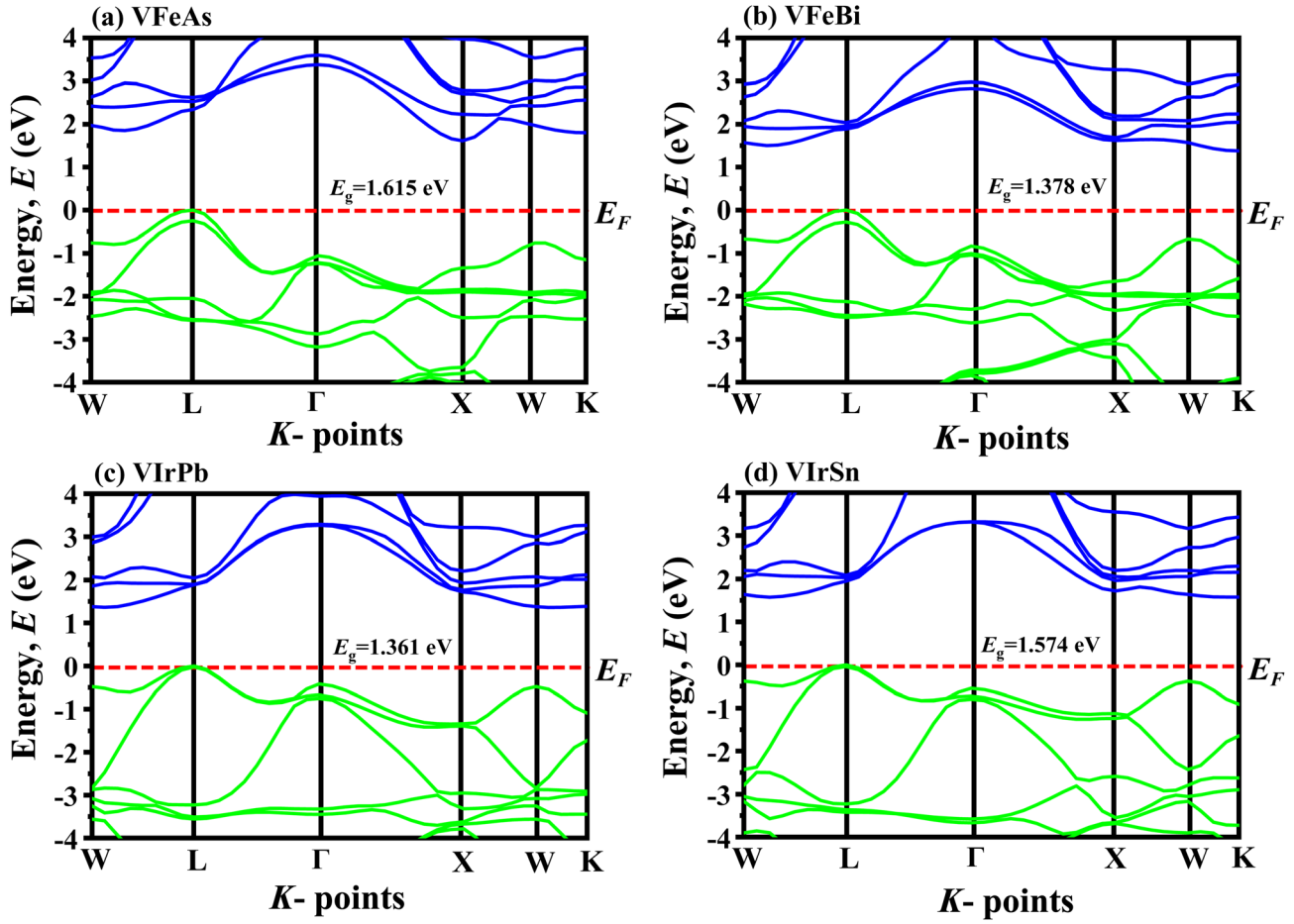

Fig. 2 The band structures of (a) VFeAs, (b) VFeBi, (c) VIrPb, and (d) VIrSn.

splitting near the Fermi level, with the strength of this effect increasing systematically for compounds containing heavier elements such as Bi, Pb, and Ir. Despite these changes, all investigated compounds retain their indirect semiconducting nature. For VFeAs, SOC induces only minor modifications to the band dispersion, resulting in a slightly reduced indirect band gap of 0.353 eV. In VFeBi, the enhanced relativistic effects associated with Bi cause more prominent valence-band splitting, decreasing the band gap to 0.066 eV. In VIrPb, SOC leads to significant splitting in both the conduction and valence bands, consistent with the presence of heavy Pb and Ir atoms, and yields a modified band gap of 0.212 eV. A similar behavior is observed in VIrSn, where SOC reduces the band gap to 0.286 eV and produces distinct splitting at several high-symmetry *k*-points. Overall, SOC reduces the band gaps and introduces additional splitting particularly in Bi- and Pb-containing compounds—yet the fundamental electronic trends and semiconducting character remain preserved. These SOC-inclusive results therefore provide a more accurate and complete description of the electronic properties of the studied Half-Heusler materials.

Fig. 4 shows the Total Density of States (TDOS) and Partial Density of States (PDOS) of VXY (X = Fe, Ir and Y = As, Bi, Pb, Sn) at absolute zero pressure and temperature. The primary contributors to the valence and conduction bands are the V-3d, Fe-3d, and As-4p orbitals for VFeAs; V-3d, Fe-3d, and Bi-6p orbitals for VFeBi; V-3d, Ir-5d, and Pb-6p orbitals for VIrPb; and V-3d, Ir-5d, and Sn-5p orbitals for VIrSn, as depicted in Fig. 4. Most of these orbitals are distributed within the energy range of −6 eV to +6 eV, indicating their key roles in determining the electronic behavior of these Heusler alloys.

In all figures, the valence and conduction bands are separated by a broken dotted line, which represents the Fermi level located at 0 eV. For VFeAs, the Fe-3d orbitals exhibit a sharp peak at approximately −2.16 eV with a density of about 4.14 states per eV, while the V-3d orbitals peak near 3.03 eV (2.25 states per eV). The As-4p orbitals contribute around −4.79 eV (1.18 states per eV). In VFeBi, the Fe-3d states dominate at −1.97 eV (4.47 states per eV), and the V-3d orbitals appear at 2.31 eV (3.11 states per eV), while the Bi-6p orbitals contribute prominently around −4.04 eV (1.18 states per eV). For VIrPb, the Ir-5d orbitals show a pronounced peak at −3.10 eV (5.28 states per eV), with the V-3d states peaking at 2.25 eV (3.25 states per eV). The Pb-6p orbitals are mainly located at −0.66 eV (0.68 states per eV). In VIrSn, the Ir-5d orbitals have a strong contribution near −3.25 eV (4.28 states per eV), while V-3d orbitals peak at 2.36 eV (3.35 states per eV). The Sn-5p orbitals are centered around −0.69 eV (0.62 states per eV). These partial

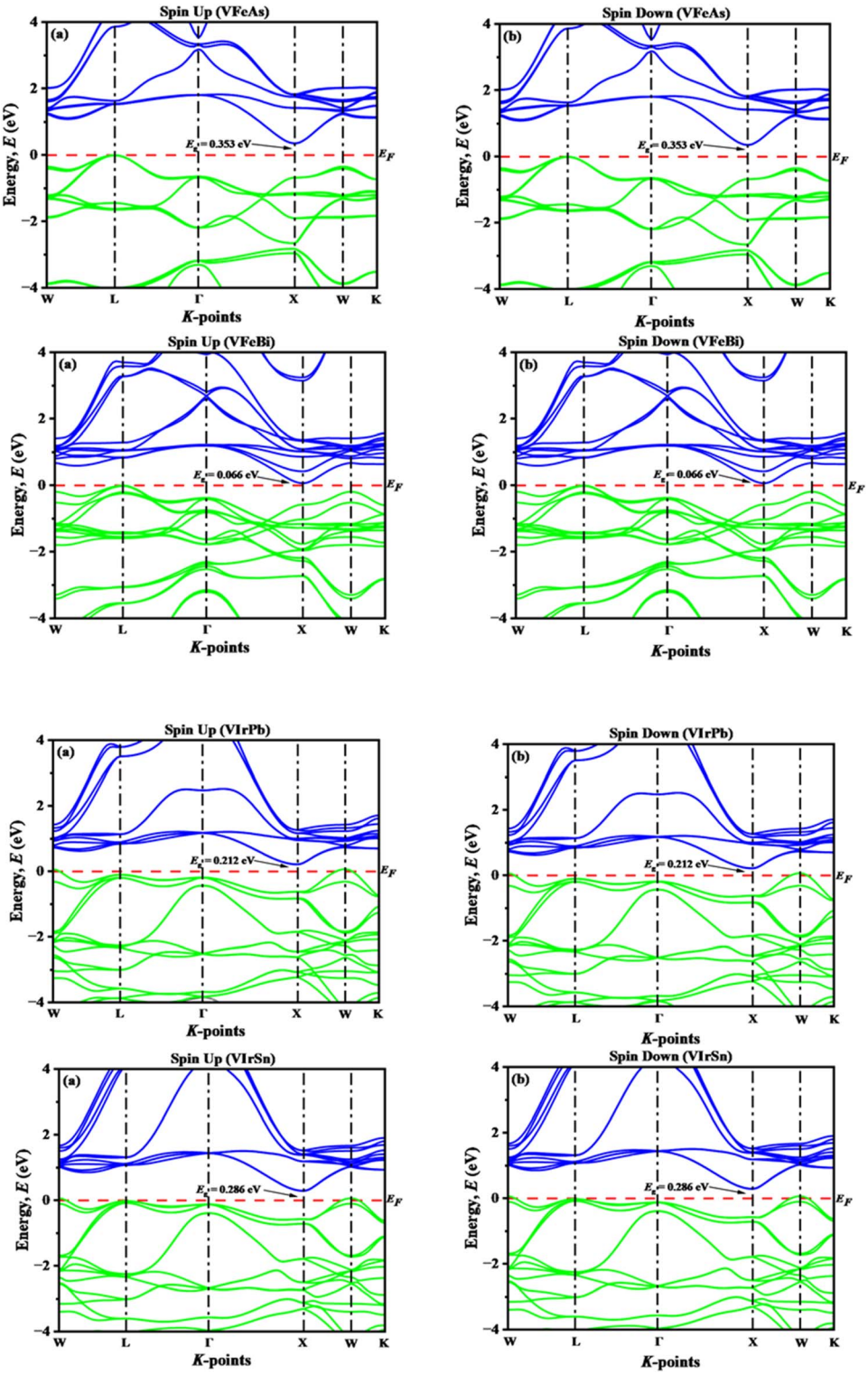

Fig. 3 Spin–Orbit Coupling (SOC) for (a) spin-up and (b) spin-down states in the Half-Heusler compounds VFeAs, VFeBi, VIrPb, and VIrSn.

density of states (PDOS) values confirm strong p–d hybridization between the main-group p-orbitals and the transition metal d-orbitals in each material, which supports covalent bonding characteristics and electronic stability. Notably, VFeAs and VIrSn exhibit slightly higher DOS intensity near the Fermi level compared to VFeBi and VIrPb, suggesting superior carrier transport and electronic activity. These properties make VFeAs and VIrSn especially promising for semiconductor and optoelectronic applications. The Fermi level is located at 0 eV, marked by a broken dotted line in all DOS figures. The band structure and DOS consistently indicate well-defined indirect band gaps for all four compounds, confirming their

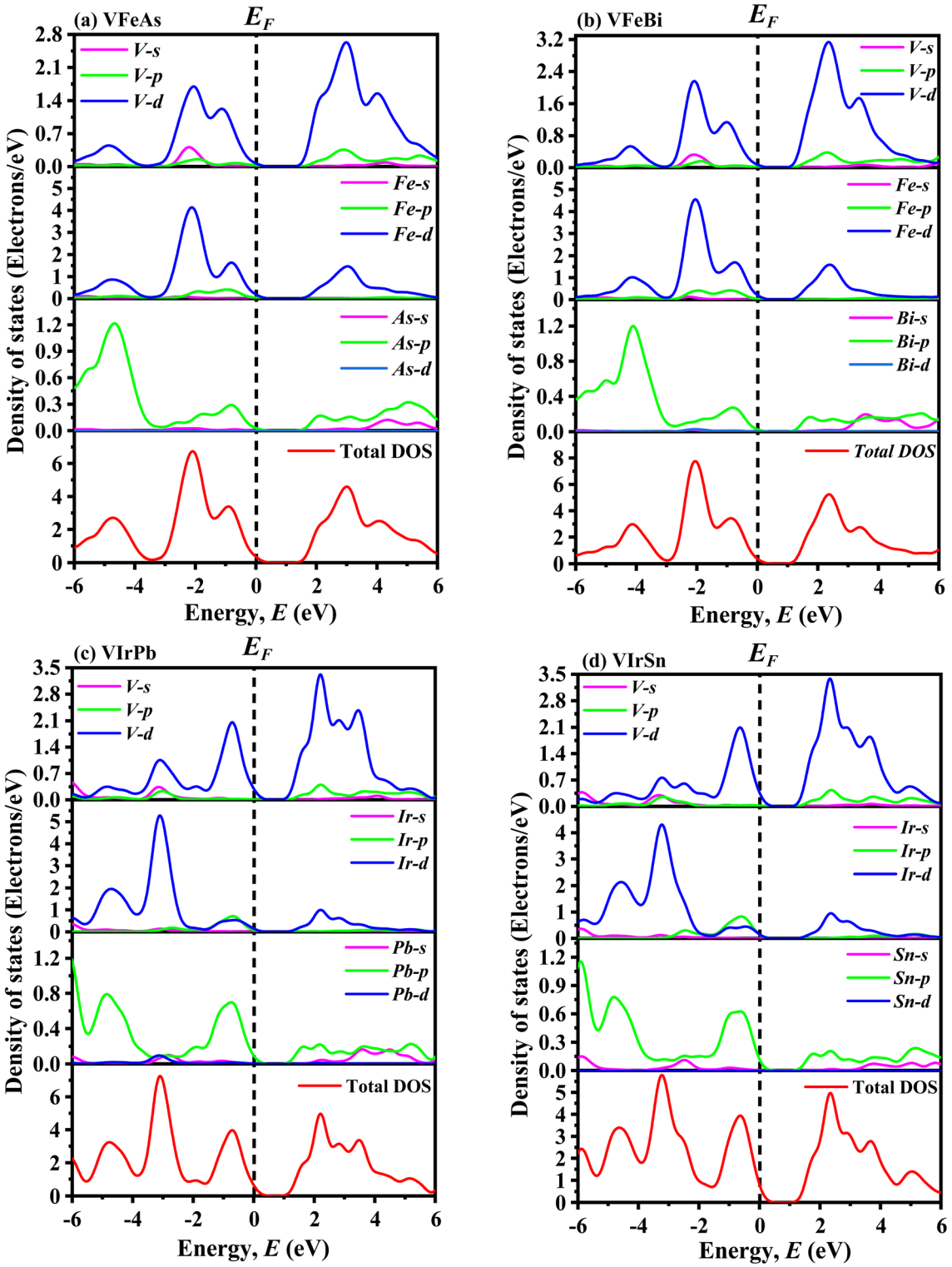

Fig. 4 PDOS and TDOS of (a) VFeAs, (b) VFeBi, (c) VIrPb, and (d) VIrSn.

semiconducting character and suggesting their suitability for optoelectronic applications. The sharp peaks in the d-orbitals near the Fermi level imply high effective masses, but also indicate strong localization and potential thermoelectric performance.[40]

3.3 Optical properties

The exploration of optical properties is an essential approach to understanding how materials interact with incident electromagnetic radiation.[41] Analyzing energy- and frequency-dependent optical responses plays a crucial role in

determining the suitability of these materials for optoelectronic and photovoltaic technologies. In this study, we investigated a range of optical parameters as functions of photon energy, extending up to 50 eV. The evaluated properties include the absorption coefficient ($\alpha(\omega)$), optical conductivity ($\sigma(\omega)$), reflectivity ($R(\omega)$), complex dielectric function ($\varepsilon(\omega)$), energy loss function ($L(\omega)$), and refractive index ($n(\omega)$). These frequency-dependent optical characteristics for the VXY (X = Fe, Ir; Y = As, Bi, Pb, Sn) compounds are illustrated in Fig. 5.

The absorption coefficient (α) is a key optical parameter that quantifies a material's capacity to absorb incident photons, directly influencing its potential for solar energy conversion in devices like photovoltaic cells.[42] It also serves as a measure of how electromagnetic radiation attenuates within the material, thereby providing insights into both optical and mechanical responses.[43] In this study, the energy-dependent absorption behavior of VXY compounds (where X = Fe, Ir and Y = As, Bi, Pb, Sn) was systematically examined. As illustrated in Fig. 5(a), each compound exhibits distinct absorption features, with notable peaks appearing around 3.70 eV for VFeAs, 3.00 eV for VFeBi, 2.60 eV for VIrPb, and 3.00 eV for VIrSn. These peaks correspond to absorption magnitudes of approximately 12.58×10^5 cm^{-1}, 11.51×10^5 cm^{-1}, 39.58×10^5 cm^{-1}, and 13.58×10^5 cm^{-1}, respectively. Such strong absorption in the visible and ultraviolet regions suggests promising applicability in optoelectronic and solar harvesting technologies. As the incident photon energy increases, the absorption intensities rise significantly, reaching maxima in the visible (VR) and ultraviolet (UV)

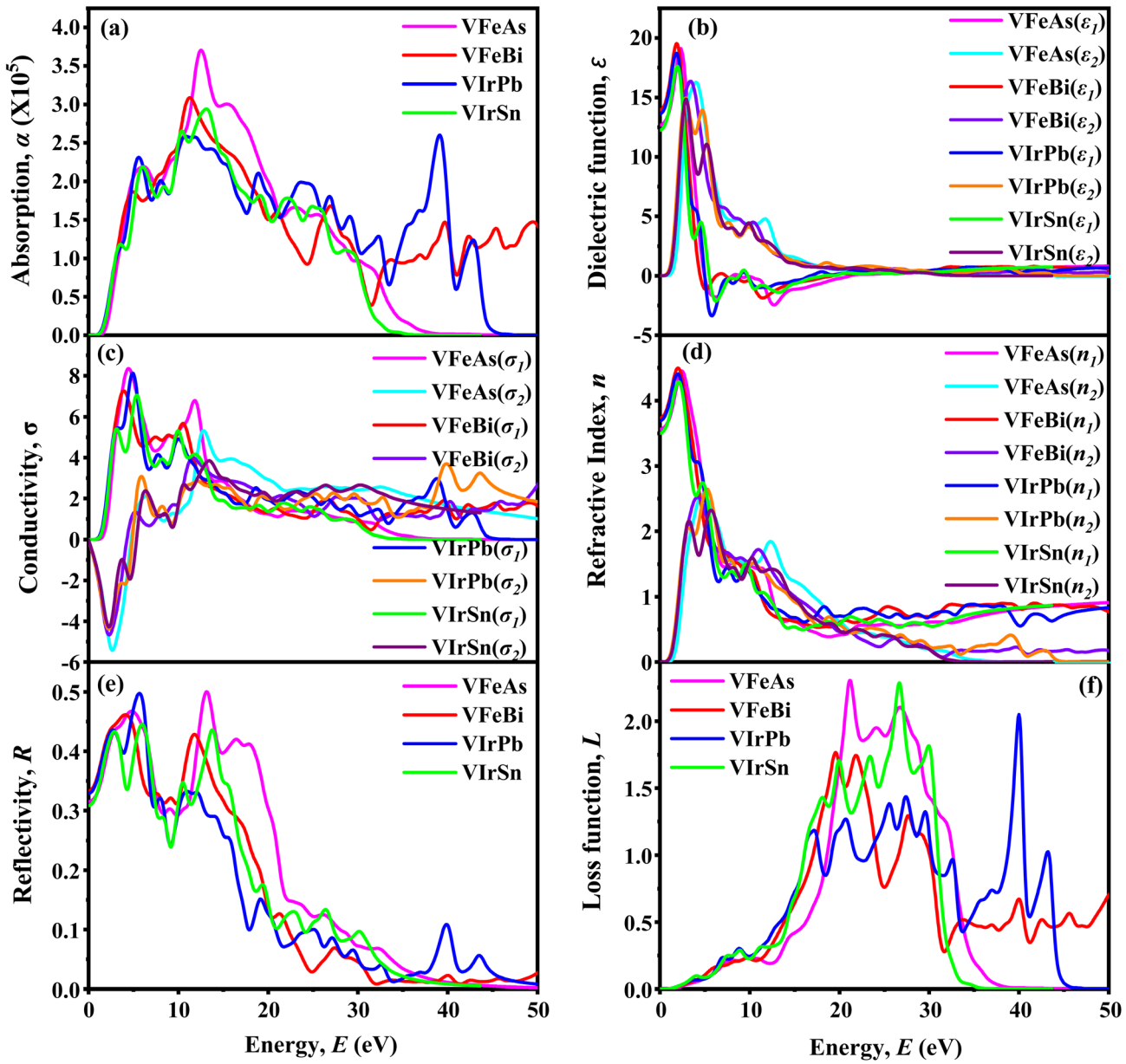

Fig. 5 Optical properties: (a) absorption, (b) dielectric function, (c) conductivity, (d) refractive index, (e) reflectivity, and (f) loss function of VXY (X = Fe, Ir; Y = As, Bi, Pb, Sn).

energy ranges, before gradually declining at higher energies. The strong absorption of VXY compounds in the visible and ultraviolet regions highlights their suitability for solar-light harvesting and UV-sensitive applications.[44] Such strong UV absorption makes them particularly attractive for use in areas like sterilization technologies, including the disinfection of surgical instruments.[45] Moreover, their notable absorption coefficients in the UV spectrum further support their potential utility in advanced technological applications, such as space-grade photovoltaic systems,[46] solid-state ultraviolet light-emitting diodes (LEDs), X-ray phosphors, and other optical and radiation detection devices.[47]

As shown in Fig. 5(b), both the real part (ε_1) and imaginary part (ε_2) of the dielectric function exhibit an increasing trend in the low-energy region as the photon energy rises.[48] However, as the energy reaches the visible region (VR), the real part ε_1 begins to decrease, while the imaginary part ε_2 shows a similar decreasing behavior in the ultraviolet region (UR). This variation in dielectric response indicates that the VXY compounds (where X = Fe, Ir and Y = As, Bi, Pb, Sn) possess strong frequency-dependent dielectric characteristics, making them suitable candidates for use in microelectronic devices and integrated circuit components.[49] The static dielectric constants for these compounds are found to range between 12.5 and 14, which aligns with values typical of materials exhibiting strong polarizability. Notably, beyond 5 eV, the real part $\varepsilon_1(\omega)$ becomes negative, suggesting that the materials enter a regime of metal-like behavior, where they reflect nearly all incident electromagnetic radiation due to the plasma frequency being exceeded. The imaginary part $\varepsilon_2(\omega)$ reaches its maximum at what is known as the first absorption peak (FAP)—an indicator of major electronic transitions near the Fermi level. For the compounds under study, the FAP values are measured to be approximately 16.00 at 3.90 eV for VFeAs, 16.00 at 3.70 eV for VFeBi, 14.00 at 3.00 eV for VIrPb, and 15.00 at 3.00 eV for VIrSn, confirming their strong absorption response in the low- to mid-UV energy range.

The optical conductivity spectra, both real and imaginary components, are illustrated in Fig. 5(c). Optical conductivity, denoted as $\sigma(\omega)$, characterizes a material's ability to transport free charge carriers under electromagnetic radiation across a specific photon energy range. The real part of $\sigma(\omega)$ reflects the material's dissipative response, essentially representing energy absorption due to electronic transitions. As depicted in the figure, the real part of the optical conductivity exhibits a noticeable rise in the energy range of approximately 3.70 to 5.40 eV, which corresponds to increased electron excitation from the valence to the conduction band, leading to the generation of free carriers. This behavior is evident across all four compounds studied, where a steep increase in $\sigma(\omega)$ occurs shortly after photon exposure, followed by a gradual decline as the photon energy continues to rise. This trend indicates a threshold-like response, where interband transitions dominate in the low to mid-energy range.[48] Meanwhile, the imaginary part of the optical conductivity initially shows a decreasing trend with rising photon energy, reflecting reduced energy storage capabilities in the medium. Interestingly, at higher energy levels, it begins to increase again, which is typically associated with high-energy electronic transitions and dynamic polarization effects. These results confirm the potential of the VXY (X = Fe, Ir; Y = As, Bi, Pb, Sn) compounds for optoelectronic applications, particularly in devices that operate under mid- to high-energy photon exposure.

The refractive index $N(\omega)$ is a critical optical property with broad relevance in technologies such as solar cells, infrared detectors, optical waveguides, and photonic crystals.[50] It consists of two parts: the real component (n), which defines the phase velocity of light through a medium, and the imaginary component (k), which reflects the extent of light absorption within the material. As presented in Fig. 5(d), the static refractive index n (0) for the studied VXY compounds (where X = Fe, Ir and Y = As, Bi, Pb, Sn) lies within the range of approximately 3.50 to 3.70. This range is considered optimal for devices such as quantum dot light-emitting diodes (QLEDs), organic LEDs (OLEDs), photovoltaic cells, and waveguides.[51] Furthermore, the peak refractive index values observed are between 4.25 and 4.50, occurring around a photon energy of 2.40 eV, indicating strong light–matter interaction in the visible energy range. Prior studies suggest that optoelectronic devices perform efficiently when the refractive index lies between 2.0 and 4.0.[52] The VXY materials investigated fall within or near this ideal window, reinforcing their promise for advanced optical and optoelectronic applications. Additionally, the fact that all refractive index values are greater than one confirms their semiconducting nature.

Reflectivity refers to the proportion of incident light that is reflected off the surface of a material in comparison to the total incoming light energy. It provides important insights into the surface optical response and energy loss characteristics of a material. As illustrated in Fig. 5(e), the reflectivity of the VXY compounds (where X = Fe, Ir and Y = As, Bi, Pb, Sn) exhibits significant values, with maximum reflectance reaching approximately 50% for VFeAs, 46% for VFeBi, 49% for VIrPb, and 44% for VIrSn. This indicates that nearly half of the incident light is reflected in the low-energy region. However, as the photon energy increases, a notable decrease in reflectivity is observed in the high-energy (UV) region. This reduction is attributed to enhanced interband electronic transitions, where photons with sufficient energy excite electrons across the band gap, thereby reducing the amount of light reflected from the material surface. Such reflectivity behavior suggests that these compounds can effectively manage light–matter interactions and may be promising candidates for applications in photonic coatings, solar absorbers, and optoelectronic surface engineering.[39]

The energy-loss function $L(\omega)$ characterizes the amount of energy dissipated by a high-energy electron as it travels through a material. The most prominent peak in the $L(\omega)$ spectrum signifies the plasma resonance, where collective oscillations of the material's free electron cloud occur. The energy corresponding to this peak is known as the plasma energy, and the associated frequency is referred to as the plasma frequency ω_p. As shown in Fig. 5(f), the VXY compounds (X = Fe, Ir; Y = As, Bi, Pb, Sn) exhibit distinct plasma peaks. Specifically, the

maximum energy-loss values are observed at 2.27 units at 21.00 eV for VFeAs, 1.72 units at 20.00 eV for VFeBi, 2.00 units at 40.00 eV for VIrPb, and 2.27 units at 26.00 eV for VIrSn. These peak values reflect the plasma resonance frequencies of the respective materials and are crucial for understanding their electronic excitation behavior and optical response in high-energy regimes. Such peaks are indicative of where the real part of the dielectric function crosses zero and the material exhibits metal-like reflective behavior, which is important for applications in plasmonic, energy filters, and radiation shielding materials.[53]

3.4 Mechanical properties

The elastic constants of a crystal are fundamental in understanding its response to external mechanical stimuli under equilibrium conditions, revealing key attributes such as mechanical robustness, ductility, brittleness, interatomic bonding strength, and hardness.[27,54] For materials with a cubic crystal structure, it is sufficient to compute only three independent elastic constants C_{11}, C_{12} and C_{44} owing to the symmetry relations (where $C_{11} = C_{22} = C_{33}$, $C_{12} = C_{23} = C_{13}$, and $C_{44} = C_{55} = C_{66}$) inherent in such systems.[30] In this study, these elastic constants were determined through the stress–strain methodology, implemented within the CASTEP simulation framework.[55] For cubic crystals to be considered mechanically stable, their elastic constants must comply with the Born mechanical stability criteria, which impose essential constraints on the magnitudes and relationships of the elastic constants.[56]

$$C_{11} - C_{12} > 0,\ C_{44} > 0 \text{ and } C_{11} + 2C_{12} > 0 \quad (8)$$

The alloys VFeAs, VFeBi, VIrPb, and VIrSn meet the aforementioned requirements, demonstrating their mechanical stability (Table 1). Subsequently, essential mechanical characteristics such as Young's modulus (Y), bulk modulus (B), shear modulus (G), and Poisson's ratio (ν) may be ascertained utilizing the Voigt–Reuss–Hill (VRH) approximations from the independent elastic constants C_{ij}.[57] The Voigt approximation is utilized to calculate the bulk modulus (B_V) and shear modulus (G_V), as seen below:

$$B_v = B_R = \frac{C_{11} + 2C_{12}}{3} \quad (9)$$

$$G_v = \frac{C_{11} - C_{12} + C_{44}}{5} \quad (10)$$

$$G_R = \frac{5C_{44}(C_{11} - C_{12})}{[4C_{44} + 3(C_{11} - C_{12})]} \quad (11)$$

As outlined by the Voigt–Reuss–Hill (VRH) approximation, the average values of the bulk modulus (B) and shear modulus (G) are expressed as follows:

$$B = \frac{1}{2}(B_R + B_v) \quad (12)$$

$$G = \frac{1}{2}(G_R + G_v) \quad (13)$$

$$Y = \frac{9BG}{3B + G} \quad (14)$$

$$\nu = \frac{3B - 2G}{2(3B + G)} \quad (15)$$

The bulk modulus (B) is a critical mechanical parameter that quantifies a material's resistance to uniform compression by evaluating the ratio of volumetric stress to strain. A higher value of B reflects greater resistance to volume change and plastic deformation. As shown in Table 3, VFeAs exhibits the highest bulk modulus among the investigated compounds, indicating its superior resistance to compressive deformation. The descending order of bulk modulus for the studied materials is: VFeAs > VIrSn > VIrPb > VFeBi. The shear modulus (G), another fundamental mechanical property, measures the resistance of a material to shape change under shear stress, indicating the strength of directional atomic bonding. A larger G value implies stronger resistance to shear deformation. According to Table 3, VFeAs again shows the highest shear modulus, suggesting more robust bonding and better mechanical stability under shear loading compared to the other compounds. The order of shear modulus values follows the trend: VFeAs > VIrSn > VFeBi > VIrPb. Furthermore, Young's modulus (Y) reflects the stiffness of a material in response to uniaxial stress and is a key indicator of its rigidity. A high Y value signifies a less deformable (*i.e.*, stiffer) material. From the data presented in Table 3, VFeAs displays the highest Young's modulus, underscoring its superior stiffness relative to the other compounds studied. The trend for Young's modulus is: VFeAs > VIrSn > VFeBi > VIrPb.

Hardness is a key macroscopic mechanical property widely utilized in materials science, particularly in industrial and

Table 3 The evaluated elastic constants C_{ij} (GPa) with Born stability criteria, Cauchy pressure, bulk modulus B (GPa), shear modulus G (GPa), Young's modulus Y (GPa), hardness H_V (GPa), machinability index ($\mu_m = B/C_{44}$), Kleinman parameter (ζ), Poisson's ratio ν, Pugh's ratio B/G, of titled compounds

Parameters		VFeAs	VFeBi	VIrPb	VIrSn
Born stability	C_{11} (GPa)	333.18	259.45	210.87	252.07
	C_{12} (GPa)	123.60	74.83	119.37	132.16
	C_{44} (GPa)	109.52	33.00	28.31	59.73
	$C_{11} - C_{12}$ (GPa)	209.58	184.62	182.56	119.91
	$C_{11} + 2C_{12}$ (GPa)	580.38	409.11	267.49	516.39
Cauchy pressure, C_P (GPa)		14.08	41.83	91.06	72.43
Bulk modulus, B (GPa)		193.46	136.37	149.87	172.13
Shear modulus, G (GPa)		107.63	56.72	34.35	59.82
Young modulus, Y (GPa)		272.38	149.45	95.73	160.83
Hardness H_V (GPa)		16.86	6.92	2.45	6.22
Machinability index ($\mu_m = B/C_{44}$)		1.76	4.13	5.29	2.88
Kleinman parameter (ζ)		0.512	0.436	0.679	0.645
Poisson's ratio, ν		0.270	0.317	0.393	0.344
Pugh's ratio, B/G		1.79	2.40	4.36	2.87

technological applications. It is primarily governed by a material's resistance to irreversible (plastic) deformation. Materials exhibiting higher hardness values demonstrate greater resilience against plastic deformation, whereas those with lower hardness tend to deform more readily under applied stress. In this study, the Vickers hardness (H_V) has been evaluated using a standard empirical relation.[58]

$$H_v = \frac{(1-v)Y}{6(1+v)} \tag{16}$$

In the hardness range of 2 to 8 GPa, materials generally exhibit enhanced machinability and resistance to mechanical damage.[59] Among the examined compounds, VFeAs displays the highest hardness value, underscoring its superior capacity to resist plastic deformation. Conversely, VIrPd presents the lowest hardness, implying better machinability relative to the other materials under consideration. Based on the values reported in Table 3, the descending order of hardness is as follows: VFeAs > VFeBi > VIrSn > VIrPd.

The internal strain response of a material can be described by the Kleinman parameter (ζ), which quantifies the material's flexibility to accommodate structural deformation, ranging between 0 and 1.[60] A lower ζ value reflects stronger resistance to external stress *via* bond stretching or contraction, whereas a higher ζ indicates that the material accommodates deformation primarily through bond angle variation (bending).[61] The Kleinman parameter is computed using the following relation:

$$\zeta = \frac{C_{11} + 8C_{12}}{7C_{11} + 2C_{12}} \tag{17}$$

As illustrated in Table 3, the mechanical strength of VFeAs, VFeBi, VIrPb, and VIrSn primarily arises from bond stretching or contraction mechanisms.

In contemporary industrial processes, a material's machinability is a critical parameter, influencing both manufacturing efficiency and overall production costs. Several factors including cutting strategies, mechanical characteristics such as stiffness and hardness, and tool design collectively impact the machinability index (μ_m).[62] The machinability index is calculated using the expression:

$$\mu_m = \frac{B}{C_{44}} \tag{18}$$

Based on the calculated values, VFeAs demonstrates a considerable machinability index, reflecting its notable mechanical competence relative to the other materials under investigation. However, a closer examination of Table 3 reveals that VIrPb exhibits the highest μ_m value among the studied compounds, indicating its superior machinability and enhanced suitability for practical industrial applications. To evaluate the ductility or brittleness of a material, Pugh's ratio (B/G) is commonly used. This ratio relates the bulk modulus (B) to the shear modulus (G), serving as a mechanical indicator of deformation behavior.[63] A B/G value greater than 1.75 suggests ductile nature, whereas values below this threshold indicate brittleness. According to the results listed in Table 3, all four compounds VFeAs, VFeBi, VIrPb, and VIrSn exhibit B/G ratios exceeding 1.75, signifying ductile characteristics. Another important parameter in assessing a material's ductility is Poisson's ratio (ν). Generally, materials with $\nu > 0.26$ are classified as ductile, while those with lower values are considered brittle.[64] All studied compounds present Poisson's ratio values exceeding 0.26, further confirming their ductile mechanical behavior.

3.5 Elastic anisotropy

Anisotropy is a vital physical property intrinsically linked to the elastic behavior of materials.[65] The degree of elastic anisotropy governs the microscopic mechanical response in both single and polycrystalline structures.[66] This characteristic has a pronounced influence on phenomena such as microscale cracking, dislocation movement, precipitation processes, plastic deformation, and phonon dispersion modes.[67] Accurate quantification of anisotropy is therefore essential in fields such as applied engineering mechanics and crystal physics.[68–71] According to the model proposed by Shivakumar Ranganathan,[72] elastic anisotropy can be quantified using the universal anisotropy index (A^U), defined as:

$$A^U = \frac{G_V}{G_R} + \frac{B_v}{B_R} - 6 \geq 0 \tag{19}$$

In this expression, $A^U = 0$ denotes an elastically isotropic material, while any deviation from zero ($A^U \neq 0$) indicates anisotropic behavior. Based on the calculated A^U values (Table 3), the compounds VFeAs, VFeBi, and VIrPb exhibit anisotropic behavior, whereas VIrSn is found to be isotropic. To provide further insight into anisotropy, Chung and Buessem[73] introduced the percent anisotropy parameters for the A_B (bulk modulus) and A_G (shear modulus), given as:

$$A_B = \frac{B_V - B_R}{B_V + B_R} \tag{20}$$

$$A_G = \frac{G_V - G_R}{G_V + G_R} \tag{21}$$

Here, A_B is associated with isotropic compression behavior, while A_G reflects the response to shear deformation. A material is considered elastically isotropic when both $A_G = A_B = 0$. The current analysis reveals that all compounds, except VIrSn, show non-zero values for these parameters, thereby confirming their anisotropic nature. For a more detailed understanding of directional shear anisotropy, the shear anisotropic factors A_1, A_2, and A_3, corresponding to the {100}, {010}, and {001} crystallographic planes, are calculated using the following relationships:

For the shear plane {100},

$$A_1 = \frac{4C_{44}}{C_{11} + C_{33} - 2C_{13}} \tag{22}$$

For the shear plane {010},

$$A_2 = \frac{4C_{55}}{C_{22} + C_{33} - 2C_{23}} \tag{23}$$

Table 4 Calculated elastic anisotropic factors (A_1, A_2, A_3, A_Z, A^U, A^{eq}, A^L) for VFeAs, VFeBi, VIrPb, and VIrSn

Compounds	A_1	A_2	A_3	A_Z	A^U	A^{eq}	A^L	Ref.
VFeAs	1.04	1.04	1.04	1.04	0.002	1.001	0.001	This study
VFeBi	0.357	0.357	0.357	0.357	1.385	2.154	0.547	
VIrPb	0.618	0.618	0.618	0.618	0.281	1.234	0.122	
VIrSn	1	1	1	1	0.00	1	0	

For the shear plane {001},

$$A_3 = \frac{4C_{66}}{C_{11} + C_{22} - 2C_{12}} \tag{24}$$

In a perfectly isotropic crystal, the values of $A_1 = A_2 = A_3 = 1$. Any deviation from unity signifies increasing anisotropy. As observed in Table 4, the shear anisotropy factors for VFeAs, VFeBi, and VIrPb deviate from unity, indicating anisotropic behavior, whereas VIrSn maintains unity values, confirming isotropic characteristics. Additional parameters such as the Zener anisotropy index (A_Z) and the equivalent Zener anisotropy factor (A^{eq}) are also evaluated to enhance the characterization of elastic anisotropy.[74,75]

$$A_Z = \frac{2C_{44}}{C_{11} - C_{12}} \tag{25}$$

A value of $A_Z = 1$ represents perfect isotropy, while deviations imply anisotropy. Table 4 shows that VFeAs, VFeBi, and VIrPb exhibit anisotropic behavior (as $A_Z \neq 1$), while VIrSn remains isotropic.

$$A^{eq} = \left(1 + \frac{5}{12}A^U\right) + \sqrt{\left(1 + \frac{5}{12}A^U\right)^2} \tag{26}$$

The value $A^{eq} = 1$ also represents isotropy. As reflected in Table 4, VFeAs, VFeBi, and VIrPb exhibit values deviating from unity, confirming their anisotropic behavior, while VIrSn remains isotropic.

To visually assess the directional dependence of Young's modulus (Y), shear modulus (G), and Poisson's ratio (ν), both 2D and 3D surface plots were generated using the ELATE program,[76] as presented in Fig. 6–9 for all compounds. In an ideal isotropic material, the 3D surface would appear as a perfect sphere; any distortion signifies anisotropy in mechanical response.[77] The evident variations in the surface geometries for each compound confirm the anisotropy discussed earlier. These graphical observations are in agreement with the computed anisotropic parameters. The minimum and maximum limits of Young's modulus, Y (GPa), shear modulus, G (GPa), and Poisson's ratio, ν for VFeAs, VFeBi, VIrPb, and VIrSn are listed in Table 5.

3.6 Thermodynamic properties

Thermodynamic parameters offer vital insights into a material's structural stability, lattice dynamics, and heat conduction performance. In this study, the Debye temperature (θ_D), melting temperature (T_m), minimum thermal conductivity (K_{min}), and Grüneisen parameter (γ) have been systematically investigated for the VXY compounds, where X = Fe, Ir and Y = As, Bi, Pb, Sn. The Debye temperature (θ_D) reflects the strength of atomic bonding and the stiffness of the crystal lattice. A higher (θ_D) value corresponds to stronger interatomic interactions and enhanced vibrational stability. The Debye temperature (θ_D) can be evaluated based on the average sound velocity (v_m), which is influenced by both the shear modulus (G) and the bulk modulus (B). The average sound velocity is calculated using the following expressions.[78]

$$v_m = \left[\frac{1}{3}\left(\frac{2}{v_t^3} + \frac{1}{v_l^3}\right)\right]^{-\frac{1}{3}} \tag{27}$$

In eqn (1), "v_t" denotes the transverse sound velocity, whereas "v_l" corresponds to the longitudinal sound velocity. These velocities are determined using the following formulas:

$$v_l = \left(\frac{B + \frac{3}{4}G}{\rho}\right) \tag{28}$$

$$v_t = \left[\frac{G}{\rho}\right]^{\frac{1}{2}} \tag{29}$$

The Debye temperature, θ_D[79] can be calculated using the following equation:

$$\theta_D = \frac{h}{k_B}\left[\frac{3n}{4\pi V}\right]^{\frac{1}{3}} v_m \tag{30}$$

Here, h denotes Planck's constant, k_B is the Boltzmann constant, V refers to the unit cell volume, n signifies the number of atoms within the unit cell, and v_m represents the material's average sound velocity under investigation. Among the four compounds, VFeAs has the highest Debye temperature at 581.53 K, indicating robust bonding and high thermal stability. This is followed by VFeBi at 336.07 K, VIrSn at 327.02 K, and VIrPb at 225.46 K, suggesting progressively weaker bonding and lower vibrational resistance. Table 6 presents the calculated Debye temperature for the VXY compounds the melting temperature (T_m) determines a material's capacity to withstand high thermal conditions without undergoing structural breakdown. Determining the melting temperature of a material is essential, as it reveals the thermal stability range in which the material can operate without undergoing oxidation, chemical changes, or major deformation due to heat. In this study, the elastic constants of the investigated materials have been utilized to

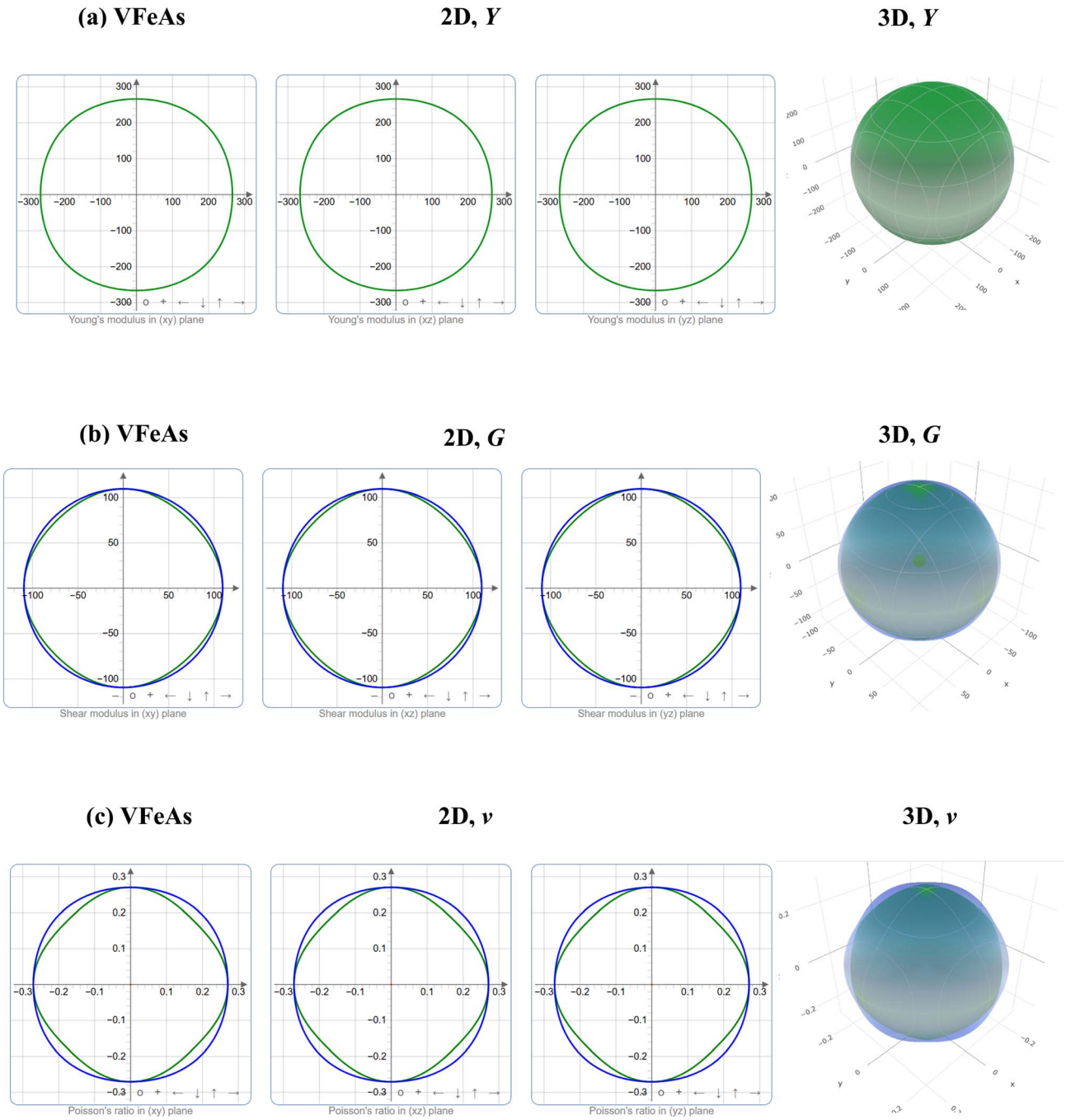

Fig. 6 3D and 2D representations of VFeAs showing (a) *Y* (Young's modulus), (b) *G* (shear modulus), and (c) *v* (Poisson's ratio).

estimate their melting temperatures (T_m) through the following equation.[51]

$$T_m = 354k + (4{\cdot}5k\ \ \mathrm{Gpa}^{-1})\left(\frac{2C_{11} + C_{33}}{3}\right) \pm 300k \qquad (31)$$

Table 6 presents the calculated melting temperatures for the VXY compounds. VFeAs again shows the highest melting point at 1517.82 K, highlighting its suitability for high-temperature applications. The melting temperatures for VIrSn, VFeBi, and VIrPb are 1199.80 K, 1181.85 K, and 1029.07 K, respectively, which aligns well with their corresponding Debye temperatures and bonding strength. The minimum thermal conductivity (K_{min}) gives the lower limit of heat conduction through the lattice and is crucial in identifying potential thermoelectric materials. The minimum thermal conductivity is estimated using the Clarke model, as outlined in ref. 25.

$$K_{min} = k_B \nu_m \left(\frac{M}{\rho N_A n}\right)^{\frac{-2}{3}} \qquad (32)$$

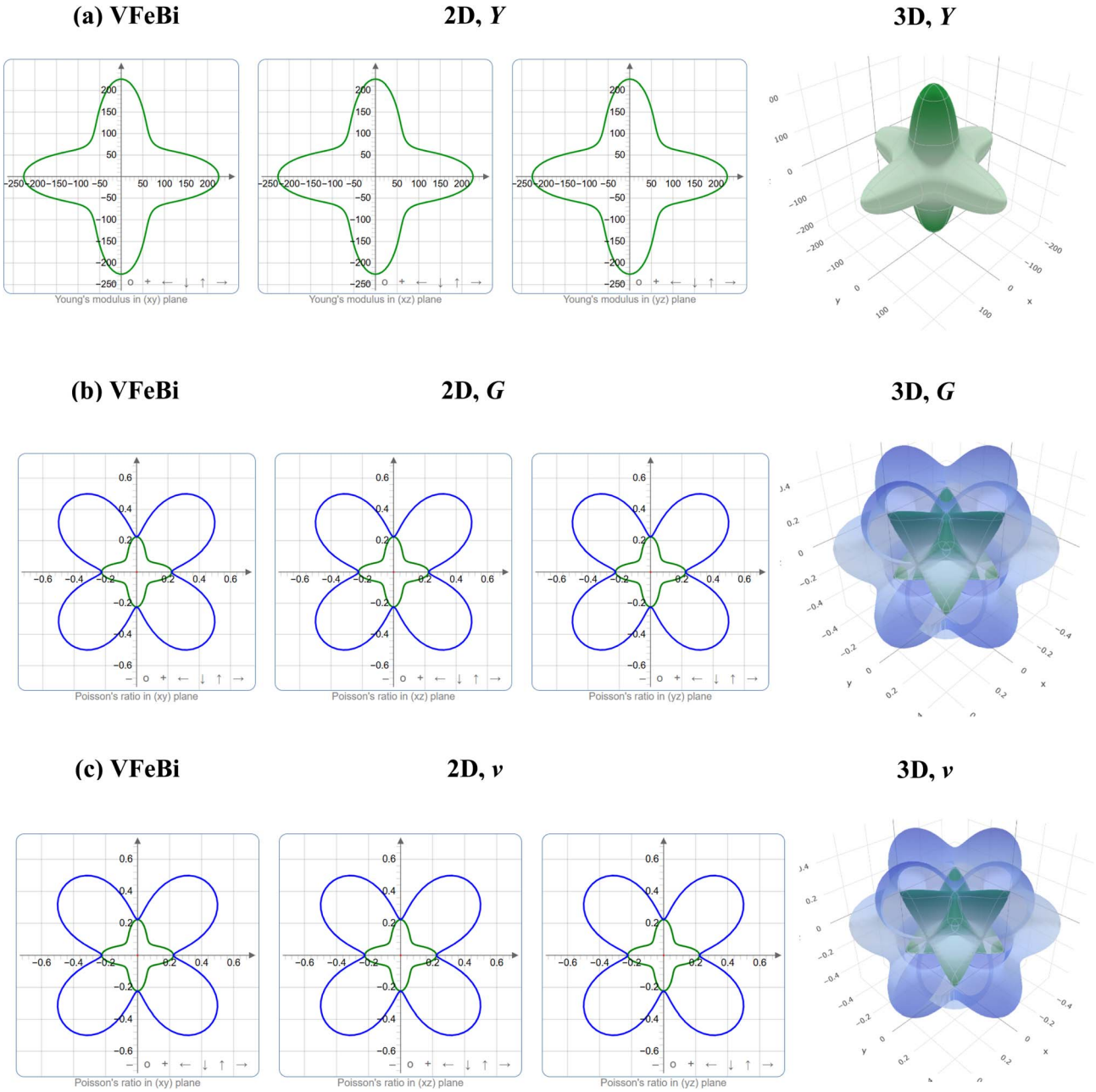

Fig. 7 3D and 2D representations of VFeBi showing (a) *Y* (Young's modulus), (b) *G* (shear modulus), and (c) *v* (Poisson's ratio).

Lower (K_{min}) implies better phonon scattering and thermal insulation capability. In this regard, VIrPb exhibits the lowest value at 0.351 W m^{-1} K^{-1}, followed by VIrSn (0.518 W m^{-1} K^{-1}), VFeBi (0.545 W m^{-1} K^{-1}), and VFeAs (1.02 W m^{-1} K^{-1}). Table 6 presents the calculated minimum thermal conductivity values for the VXY compounds. The relatively low values of K_{min} and θ_D suggest that VXY have potential as thermal barrier coating (TBC) materials, as these properties indicate their ability to reduce heat transfer and enhance thermal insulation. The Grüneisen parameter (γ) is an indicator of the anharmonicity of lattice vibrations and is closely related to thermal expansion, phonon–phonon scattering, and lattice instability. The Grüneisen parameter is widely used in solid-state physics to explore the characteristic energy scales related to changes in external potentials.[24] A larger γ value indicates a higher level of anharmonicity in the material. For the VXY compounds (where X = Fe, Ir and Y = As, Bi, Pb, Sn), the Grüneisen parameter is determined using Poisson's ratio based on the following expression.[24]

$$\gamma = \frac{3(1+v)}{2(2-3v)} \tag{33}$$

Higher values of γ typically signify more significant anharmonic effects and reduced thermal conductivity. The computed γ values for the compounds are as follows: VFeAs: 1.60, VFeBi:

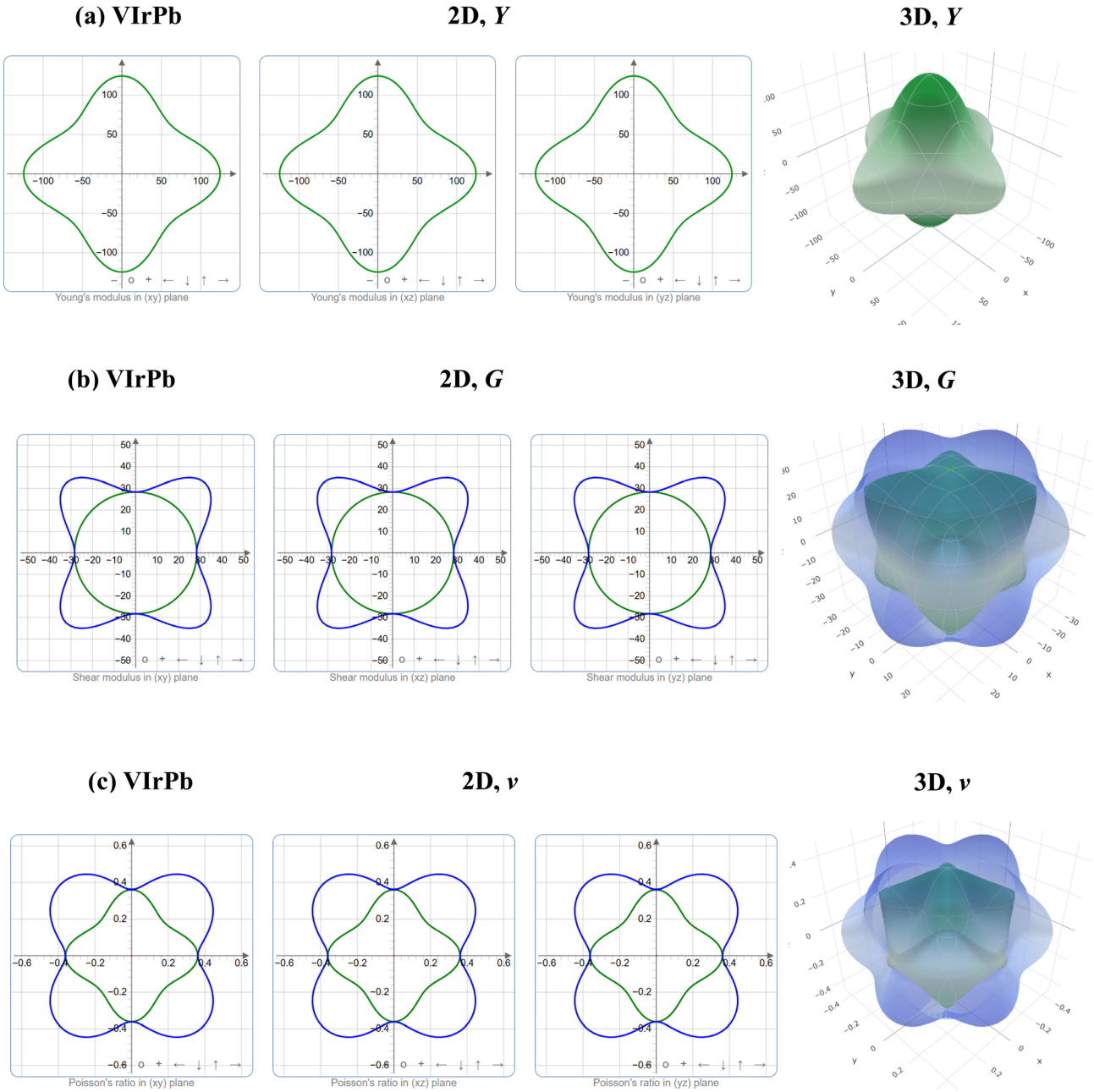

Fig. 8 3D and 2D representations of VIrPb showing (a) *Y* (Young's modulus), (b) *G* (shear modulus), and (c) *v* (Poisson's ratio).

1.88, VIrSn: 2.08, and VIrPb: 2.52. Notably, VIrPb has the highest Grüneisen parameter, indicating strong lattice anharmonicity, which contributes to its exceptionally low thermal conductivity. Conversely, VFeAs, with the lowest γ, exhibits the most harmonic lattice behavior, in line with its high Debye temperature and thermal stability.

3.7 AIMD study

In this section, we examine the *ab initio* molecular dynamics (AIMD) behavior of the vanadium-based Half-Heusler compounds VXY (X = Fe, Ir and Y = As, Bi, Pb, Sn). The simulations were performed for a total duration of 10 000 fs using the *NVE* ensemble.[80] Fig. 10(a–d) displays the temperature and total-energy variations of the compounds VFeAs, VFeBi, VIrPb, and VIrSn during the simulation.

The AIMD profile of VFeAs in Fig. 10(a) shows temperature oscillations around a stable average value without any abrupt thermal spikes, indicating the absence of structural instability. The total energy remains nearly constant, exhibiting only minor fluctuations throughout the simulation, confirming that VFeAs maintains its structural integrity under the applied thermal conditions.

Fig. 10(b) illustrates the behavior of VFeBi, which follows a similar stability trend. Although its energy decreases slightly

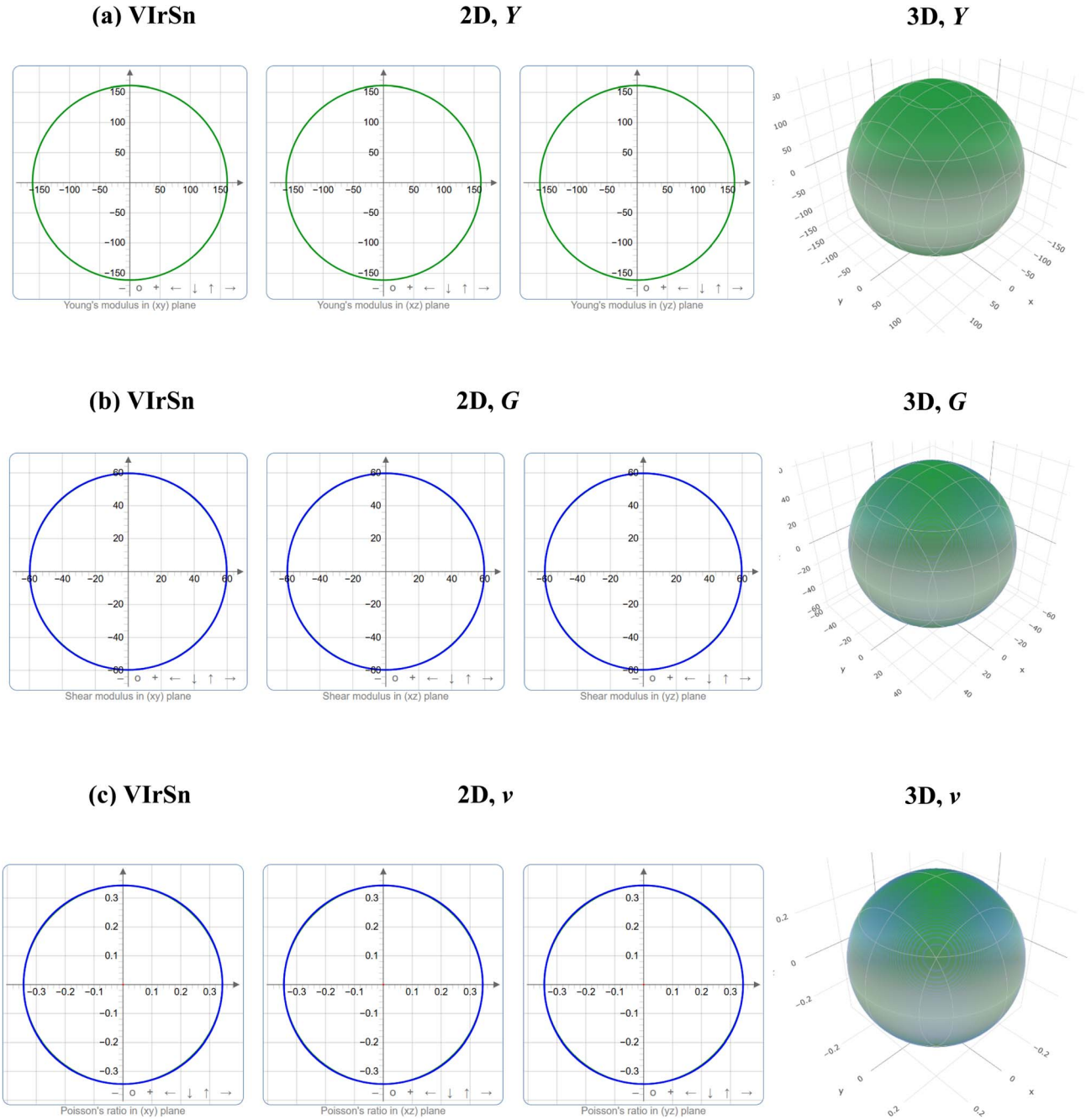

Fig. 9 3D and 2D representations of VFeAs showing (a) *Y* (Young's modulus), (b) *G* (shear modulus), and (c) *v* (Poisson's ratio).

Table 5 The minimum and maximum limits of Young's modulus, *Y* (GPa), shear modulus, *G* (GPa), and Poisson's ratio, *v* for VFeAs, VFeBi, VIrPb, and VIrSn

	Young's modulus		Shear modulus		Poisson's ratio		
Compounds	Y_{min}	Y_{max}	G_{min}	G_{max}	ν_{min}	ν_{max}	Ref.
VFeAs	266.29	276.42	104.79	109.53	0.249	0.278	This study
VFeBi	91.62	225.95	33.00	92.31	0.106	0.630	
VIrPb	79.92	124.57	28.31	45.75	0.254	0.550	
VIrSn	160.62	161.16	59.73	59.95	0.343	0.345	

Table 6 Calculated values of thermal factors of VXY (X = Fe, Ir and Y = As, Bi, Pb, Sn)

Parameter	VFeAs	VFeBi	VIrPb	VIrSn
ρ (g cm^{-3})	7.37	10.01	12.61	10.69
v_t (km s^{-1})	3.82	2.38	1.65	2.36
v_l (km s^{-1})	6.76	4.60	3.93	4.85
v_m (km s^{-1})	4.24	2.66	1.86	2.65
θ_D (k)	581.53	336.07	225.46	327.02
K_{min} (W m^{-1} K^{-1})	1.02	0.545	0.351	0.518
γ	1.60	1.88	2.52	2.08
T_m (K)	1517.82	1181.85	1029.07	1199.80

at the beginning due to an initial relaxation process, the system quickly stabilizes and continues with regular oscillations for the remainder of the simulation. Both temperature and energy remain well controlled, demonstrating that VFeBi reaches equilibrium and maintains dynamical stability.

For VIrPb, shown in Fig. 10(c), the temperature exhibits moderate, well-bounded fluctuations with no evidence of thermal instability. The total-energy curve displays somewhat larger oscillations than the Fe-based compounds, yet it remains confined within a stable range without any drift, confirming that VIrPb preserves its structural stability throughout the 10 000 fs simulation.

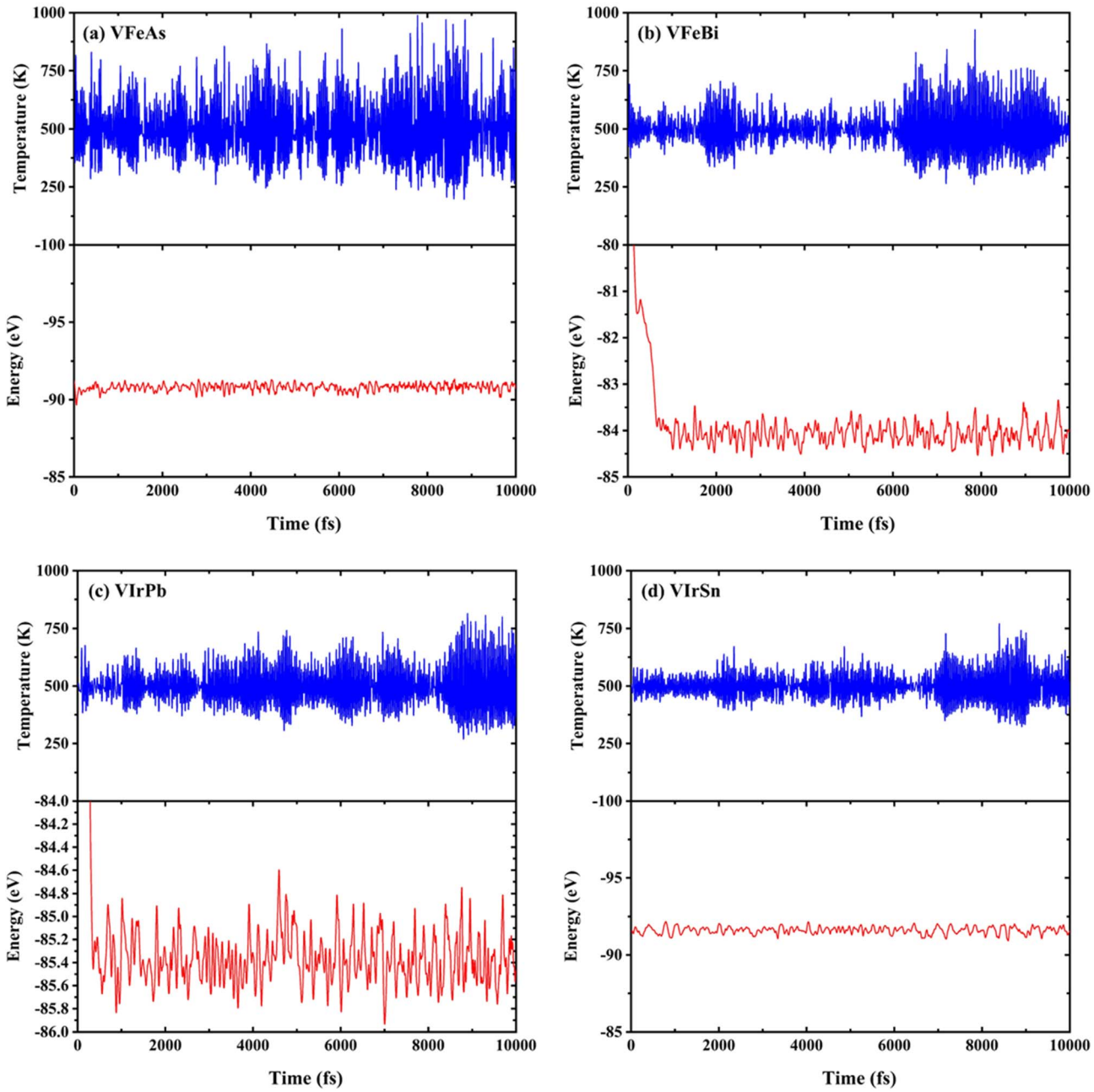

Fig. 10 *Ab initio* molecular dynamics (AIMD) temperature and total-energy profiles of vanadium-based Half-Heusler compounds: (a) VFeAs, (b) VFeBi, (c) VIrPb, and (d) VIrSn.

The AIMD behavior of VIrSn in Fig. 10(d) reveals highly stable temperature variations with a relatively narrow fluctuation range. Its energy profile is notably steady, showing very small deviations over time, which reflects excellent dynamical stability. Among all the studied compounds, VIrSn demonstrates one of the most stable energy responses, highlighting its strong thermal reliability.

4. Conclusion

This investigation leverages Density Functional Theory (DFT) to conduct a thorough first-principles examination of the electronic, mechanical, optical, and thermodynamic characteristics of VXY Half-Heusler alloys, where X represents Fe or Ir and Y denotes As, Bi, Pb, or Sn. Our computational results reveal specific lattice constants for selected compounds: VFeAs measures 5.46 Å, VFeBi at 5.88 Å, VIrPb at 6.19 Å, and VIrSn at 6.08 Å. A detailed analysis of their electronic structures consistently classifies all VXY compounds within this series (X = Fe, Ir; Y = As, Bi, Pb, Sn) as semiconductors, positioning them as promising candidates for a range of optoelectronic applications. From a mechanical perspective, our comprehensive evaluations confirm the inherent stability of these materials. Furthermore, their demonstrated ductility is a pertinent attribute for practical implementation. While assessed using the universal anisotropic index (A^U) and Zener's anisotropy index (A_Z), the elastic anisotropy assessments clearly indicate that these VXY alloys exhibit distinct elastic anisotropy, rather than isotropy. Extensive studies of their optical properties underscore excellent photoconductive behavior and high optical reflectivity. These findings strongly support their utility in diverse fields such as solar cells, waveguides, optoelectronics, and microelectronics. Additionally, the remarkably low minimum thermal conductivity (K_{min}) and reduced Debye temperature (θ_D) observed in these alloys suggest their strong suitability for thermal barrier coating (TBC) applications. VXY (X = Fe, Ir; Y = As, Bi, Pb, Sn) compounds explored in this study present considerable promise for driving significant progress across various cutting-edge domains, including green energy technologies, quantum computing, sensor development, and both spintronics and optoelectronics.

Author contributions

Md. Tarekuzzaman: investigation, methodology, data curation, software, conceptualization, writing the original manuscript; Salah Uddin: formal analysis, methodology, data curation, conceptualization, review – editing; Md. Shahazan Parves: formal analysis, methodology, data curation, conceptualization, review – editing; Fahad Alhashmi Alamer: formal analysis, data curation, review – editing; Omar Alsalmi: formal analysis, data curation, review – editing; Md. Zahid Hasan: formal analysis, validation, supervision, review – editing.

Conflicts of interest

There is no conflict to declare.

Data availability

Relevant data from this study are available from the corresponding author upon a reasonable request.

Acknowledgements

The authors extend their appreciation to Umm Al-Qura University, Saudi Arabia for funding this research work through grant number: 25UQU4290253GSSR01.

References

1 K. Manna, Y. Sun, L. Muechler, J. Kübler and C. Felser, Heusler, Weyl and Berry, *Nat. Rev. Mater.*, 2018, 244–256, DOI: 10.1038/s41578-018-0036-5.
2 *Heusler Alloys: Properties, Growth, Applications*, ed. C. Felser and A. Hirohata, Springer International Publishing, Cham, 2016.
3 P. J. Webster, *Contemp. Phys.*, 1969, **10**, 559.
4 T. Graf, C. Felser and S. S. Parkin, Simple Rules for the Understanding of Heusler Compounds, *Prog. Solid State Chem.*, 2011, 1–50, DOI: 10.1016/j.progsolidstchem.2011.02.001.
5 A. Hirohata, M. Kikuchi, N. Tezuka, K. Inomata, J. S. Claydon, Y. B. Xu and G. Van der Laan, Heusler Alloy/Semiconductor Hybrid Structures, *Curr. Opin. Solid State Mater. Sci.*, 2006, 93–107, DOI: 10.1016/j.cossms.2006.11.006.
6 T. Klimczuk, C. H. Wang, K. Gofryk, F. Ronning, J. Winterlik, G. H. Fecher, J.-C. Griveau, E. Colineau, C. Felser, J. D. Thompson, D. J. Safarik and R. J. Cava, *Phys. Rev. B: Condens. Matter Mater. Phys.*, 2012, **85**, 174505.
7 J. Kübler, A. R. William and C. B. Sommers, *Phys. Rev. B: Condens. Matter Mater. Phys.*, 1983, **28**, 1745.
8 B. Yan and A. De Visser, Half-Heusler Topological Insulators, *MRS Bull.*, 2014, 859–866, DOI: 10.1557/mrs.2014.198.
9 H. C. Kandpal, G. H. Fecher and C. Felser, *J. Phys. D: Appl. Phys.*, 2007, **40**, 1507.
10 O. E. Osafile and J. O. Umukoro, *Mol. Phys.*, 2021, **119**, e1936249.
11 F. Casper, T. Graf, S. Chadov, B. Balke and C. Felser, Half-Heusler Compounds: Novel Materials for Energy and Spintronic Applications, *Semicond. Sci. Technol.*, 2012, 063001, DOI: 10.1088/0268-1242/27/6/063001.
12 A. Szytuła, Ž. Dimitrijević, J. Todorović, A. Kołodziejczyk, J. Szelag and A. Wanic, *Phys. Status Solidi A*, 1972, **9**, 97.
13 B. Gurunani, S. Ghosh and D. C. Gupta, Comprehensive Investigation of Half Heusler Alloy: Unveiling Structural, Electronic, Magnetic, Mechanical, Thermodynamic, and Transport Properties, *Intermetallics*, 2024, 108311, DOI: 10.1016/j.intermet.2024.108311.
14 Y. Al-Douri and M. Ameri, Physical studies of spintronics-based Heusler alloys, *Crit. Rev. Solid State Mater. Sci.*, 2025, **50**, 189, DOI: 10.1080/10408436.2024.2407463.

15 L. Cheng, Q. Xiang, Y. Liao and H. Zhang, CdS-Based Photocatalysts, *Energy Environ. Sci.*, 2018, 1362–1391, DOI: 10.1039/C7EE03640J.
16 M. R. Azin-Sanjabod, B. Nedaee-Shakarab, Y. Azizian-Kalandaragh and H. Akbari, *Int. Nano Lett.*, 2021, **11**, 125.
17 J. Ma, V. I. Hegde, K. Munira, Y. Xie, S. Keshavarz, D. T. Mildebrath, C. Wolverton, A. W. Ghosh and W. H. Butler, *Phys. Rev. B*, 2017, **95**, 024411.
18 O. Polat, M. Horák, J. A. Arregi, K. Bukvišová, J. Zlámal and T. Šikola, Synthesis and Characterization of Half-Heusler ScPtBi Films via Three-Source Magnetron Co-Sputtering on Nb Superconductor Buffer Layer, *Int. Nano Lett.*, 2023, 103118, DOI: 10.1016/j.surfin.2023.103118.
19 M. Yusuf, G. S. Manyali and F. O. Saouma, Computational Study of LiAlSi, LiAlGe and LiGaSi Half-Heusler Alloys for Opto-Electronic Applications, *Phys. B*, 2024, 416390, DOI: 10.1016/j.physb.2024.416390.
20 E. Tindibale, W. M. Mulwa and B. I. Adetunji, Elastic, Anisotropic, Lattice Dynamics and Electronic Properties of XNiM and XNi2M (X= Ti, Zr, Hf; M= Sn, Ge, Si): DFT Comparison Study, *Phys. B*, 2023, 415029, DOI: 10.1016/j.physb.2023.415029.
21 G. Joshi, R. He, M. Engber, G. Samsonidze, T. Pantha, E. Dahal, K. Dahal, J. Yang, Y. Lan and B. Kozinsky, NbFeSb-Based p-Type Half-Heuslers for Power Generation Applications, *Energy Environ. Sci.*, 2014, 4070–4076, DOI: 10.1039/C4EE02180K.
22 T. Zhu, C. Fu, H. Xie, Y. Liu and X. Zhao, *Adv. Energy Mater.*, 2015, **5**, 1500588.
23 A. Amudhavalli, R. R. Palanichamy, R. Madhavan and K. Iyakutti, First Principles Study of Co and Ni Based Half Heusler Alloys, *Mater. Sci. Semicond. Process.*, 2022, 106908, DOI: 10.1016/j.mssp.2022.106908.
24 F. F. Tafti, T. Fujii, A. Juneau-Fecteau, S. René De Cotret, N. Doiron-Leyraud, A. Asamitsu and L. Taillefer, *Phys. Rev. B: Condens. Matter Mater. Phys.*, 2013, **87**, 184504.
25 A. K. Singh, S. D. Ramarao and S. C. Peter, Rare-Earth Based Half-Heusler Topological Quantum Materials: A Perspective, *APL Mater.*, 2020, **8**, 060903, DOI: 10.1063/5.0006118.
26 S. J. Clark, M. D. Segall, C. J. Pickard, P. J. Hasnip, M. I. J. Probert, K. Refson and M. C. Payne, *Z. Kristallogr. Cryst. Mater.*, 2005, **220**, 567.
27 J. P. Perdew, K. Burke and M. Ernzerhof, *Phys. Rev. Lett.*, 1996, **77**, 3865.
28 H. J. Monkhorst and J. D. Pack, *Phys. Rev. B*, 1976, **13**, 5188.
29 T. H. Fischer and J. Almlof, *J. Phys. Chem.*, 1992, **96**, 9768.
30 B. G. Pfrommer, M. Côté, S. G. Louie and M. L. Cohen, Relaxation of Crystals with the Quasi-Newton Method, *J. Comput. Phys.*, 1997, 233–240, DOI: 10.1006/jcph.1996.5612.
31 J. Heyd, G. E. Scuseria and M. Ernzerhof, Hybrid Functionals Based on a Screened Coulomb Potential, *J. Chem. Phys.*, 2003, 8207–8215, DOI: 10.1063/1.1564060.
32 M. Tarekuzzaman, M. H. Ishraq, M. A. Rahman, A. Irfan, M. Z. Rahman, M. S. Akter, S. Abedin, M. A. Rayhan, M. Rasheduzzaman, M. M. Hossen and M. Z. Hasan, *J. Comput. Chem.*, 2024, 2476–2500, DOI: 10.1002/jcc.27455.
33 M. Tarekuzzaman, M. S. I. Babu, M. A. Rayhan, S. Ahmad, M. Rasheduzzaman, M. S. H. Choudhury, M. M. Hossen, S. Nasrin and M. Z. Hasan, *Phys. Scr.*, 2024, **99**, 105920.
34 M. Islam and M. A. R. Sheikh, *Phys. B*, 2023, **668**, 415244.
35 W. Feng, D. Xiao, Y. Zhang and Y. Yao, *Phys. Rev. B: Condens. Matter Mater. Phys.*, 2010, **82**, 235121.
36 K. Bilińska and M. J. Winiarski, *Solid State Commun.*, 2023, **364**, 115133.
37 G. Vaitheeswaran, V. Kanchana, A. Svane and A. Delin, *J. Phys.: Condens. Matter*, 2007, **19**, 326214.
38 M. Saeed, M. A. Ali, S. Murad, R. Ullah, T. Alshahrani, A. Laref and G. Murtaza, Pressure Induced Structural, Electronic, Optical and Thermal Properties of CsYbBr3, a Theoretical Investigation, *J. Mater. Res. Technol.*, 2021, 687–696, DOI: 10.1016/j.jmrt.2020.12.052.
39 T. Zheng, S. Fang, J. Wang, Z. Yang, X. Yang, S. Zhao, G. Zhang, F. Luo, H. Yang, Y. S. Ang, J. Lu, X. Yang, Y. Wang and C. Wang, Layer Dependence and Point Defect for Sub-5 Nm 2D Hydrogenated GaN Transistors, *ACS Appl. Electron. Mater.*, 2025, 7(22), 10237–10251, DOI: 10.1021/acsaelm.5c01648.
40 Z. Yang, X. Yang, J. Wang, Q. Li, R. Peng, C. H. Lee, L. K. Ang, J. Lu, Y. S. Ang and S. Fang, Unconventional Thickness Scaling of Coherent Tunnel Magnetoresistance in Altermagnets, *Phys. Rev. B*, 2025, **112**(20), 205202, DOI: 10.1103/2thy-fzzj.
41 S. Huang, R.-Z. Li, S.-T. Qi, B. Chen and J. Shen, A Theoretical Study of the Elastic and Thermal Properties of ScRu Compound under Pressure, *Phys. Scr.*, 2014, 065702, DOI: 10.1088/0031-8949/89/6/065702.
42 S. Lee, A. Pirogov, M. Kang, K.-H. Jang, M. Yonemura, T. Kamiyama, S.-W. Cheong, F. Gozzo, N. Shin and H. Kimura, Giant Magneto-Elastic Coupling in Multiferroic Hexagonal Manganites, *Nature*, 2008, 805–808, DOI: 10.1038/nature06507.
43 I. G. Lezama, A. Arora, A. Ubaldini, C. Barreteau, E. Giannini, M. Potemski and A. F. Morpurgo, Indirect-to-Direct Band Gap Crossover in Few-Layer $MoTe_2$, *Nano Lett.*, 2015, **15**(4), 2336–2342, DOI: 10.1021/nl5045007.
44 A. M. Reza and S. H. Naqib, DFT Based Investigation of Bulk Mechanical, Thermophysical and Optoelectronic Properties of PbTaSe2 Topological Semimetal, *Comput. Condens. Matter*, 2023, e00833, DOI: 10.1016/j.cocom.2023.e00833.
45 I. A. Apon, R. Hasan and I. A. Ovi, Pressure-Driven Semiconducting to Metallic Transition in Francium Tin Trihalides Perovskite with Improved Optoelectronic Performance: A DFT Study, *AIP Adv.*, 2024, **14**, 065126, DOI: 10.1063/5.0207336.
46 N. Ahmed, J. Nisar, R. Kouser, A. G. Nabi, S. Mukhtar, Y. Saeed and M. H. Nasim, Study of Electronic, Magnetic and Optical Properties of KMS2 (M= Nd, Ho, Er and Lu): First Principle Calculations, *Mater. Res. Express*, 2017, 065903, DOI: 10.1088/2053-1591/aa75fc.
47 M. R. Hasan, I. A. Apon, M. M. Islam, A. U. Azad, M. Aminuzzman and M. S. Haque, DFT Based Analysis of Pressure Driven Mechanical, Opto-Electronic, and Thermoelectric Properties in Lead-Free InGeX3 (X= Cl, Br)

Perovskites for Solar Energy Applications, *AIP Adv.*, 2024, **14**, 115109, DOI: 10.1063/5.0233863.
48 T. Urata, W. Hattori and H. Ikuta, High Mobility Charge Transport in a Multicarrier Altermagnet CrSb, *Phys. Rev. Mater.*, 2024, **8**(8), 084412, DOI: 10.1103/PhysRevMaterials.8.084412.
49 Z. Yang, D. Shi, B. Wen, R. Melnik, S. Yao and T. Li, First-Principle Studies of ca–x (X= Si, Ge, Sn, Pb) Intermetallic Compounds, *J. Solid State Chem.*, 2010, 136–143, DOI: 10.1016/j.jssc.2009.11.007.
50 H. Fu, D. Li, F. Peng, T. Gao and X. Cheng, Ab Initio Calculations of Elastic Constants and Thermodynamic Properties of NiAl under High Pressures, *Comput. Mater. Sci.*, 2008, 774–778, DOI: 10.1016/j.commatsci.2008.05.026.
51 G. A. Slack, *Solid State Phys.*, 1979, **34**, 1.
52 H. H. Hegazy, G. M. Mustafa, A. Nawaz, N. A. Noor, A. Dahshan and I. Boukhris, Tuning of Direct Bandgap of Rb2ScTlX6 (X= Cl, Br, I) Double Perovskites through Halide Ion Substitution for Solar Cell Devices, *J. Mater. Res. Technol.*, 2022, 1271–1281, DOI: 10.1016/j.jmrt.2022.05.082.
53 P. B. Johnson and R. W. Christy, *Phys. Rev. B*, 1972, **6**, 4370.
54 D. Liu, S. Fang, Y. Luo, C. Zhou, J. Xu and M. Zhang, Yttrium-Doping-Induced Ferroelectric Semiconductor-to-Semimetal Phase Transition in α-In_2 Se_3 van Der Waals Bilayers, *J. Phys. Chem. C*, 2025, **129**(33), 15018–15028, DOI: 10.1021/acs.jpcc.5c02979.
55 R. Gaillac, P. Pullumbi and F.-X. Coudert, ELATE: An Open-Source Online Application for Analysis and Visualization of Elastic Tensors, *J. Phys.: Condens. Matter*, 2016, 275201, DOI: 10.1088/0953-8984/28/27/275201.
56 K. M. Hossain, M. Z. Hasan and M. L. Ali, Understanding the Influences of Mg Doping on the Physical Properties of SrMoO3 Perovskite, *Results Phys.*, 2020, 103337, DOI: 10.1016/j.rinp.2020.103337.
57 N. A. Teli and M. M. S. Sirajuddeen, A DFT Study of the Structural, Elastic, Electronic and Magnetic Properties of New Quaternary Compounds TiHfOsX (Al, Ga, In), *Phys. Lett. A*, 2020, 126793, DOI: 10.1016/j.physleta.2020.126793.
58 F. D. Murnaghan, Finite Deformations of an Elastic Solid, *Am. J. Math.*, 1937, 235–260, DOI: 10.2307/2371405.
59 F. Mouhat and F.-X. Coudert, *Phys. Rev. B: Condens. Matter Mater. Phys.*, 2014, **90**, 224104.
60 D. H. Chung and W. R. Buessem, The Elastic Anisotropy of Crystals, *J. Appl. Phys.*, 1967, 2010–2012, DOI: 10.1063/1.1709819.
61 X. Gao, Y. Jiang, R. Zhou and J. Feng, Stability and Elastic Properties of Y–C Binary Compounds Investigated by First Principles Calculations, *J. Alloys Compd.*, 2014, 819–826, DOI: 10.1016/j.jallcom.2013.11.005.
62 R. Hill, *Proc. Phys. Soc., Sect. A*, 1952, **65**, 349.
63 T. S. Nashia, M. H. Mim, M. Tarekuzzaman, S. Uddin, O. Alsalmi, H. Al-Dmour, M. Rasheduzzaman, M. S. H. Choudhury and M. Z. Hasan, Computational Investigation of LiMgZ Half-Heusler Phases Where Z = P, as, and Bi for Optoelectronic and Photoelectronic Applications, *Sci. Rep.*, 2025, **15**(1), 33943, DOI: 10.1038/s41598-025-10593-y.
64 S. F. Pugh, *London, Edinburgh Dublin Phil. Mag. J. Sci.*, 1954, **45**, 823.
65 J. Hassan, M. A. Masum and S. H. Naqib, A Comparative Ab-Initio Investigation of the Physical Properties of Cubic Laves Phase Compounds XBi2 (X= K, Rb), *Comput. Condens. Matter*, 2024, e00905, DOI: 10.1016/j.cocom.2024.e00905.
66 L. Kleinman, *Phys. Rev.*, 1962, **128**, 2614.
67 S. Uddin, A. Das, M. A. Rayhan, S. Ahmad, R. M. Khokan, M. Rasheduzzaman, R. Das, A. Ullah, Y. Arafat and M. Z. Hasan, Theoretical Prediction of the Mechanical, Electronic, Optical and Thermodynamic Properties of Antiperovskites A3BO (A = K, Rb and B = Au, Br) Using DFT Scheme: New Candidate for Optoelectronic Devices Application, *J. Comput. Electron.*, 2024, **23**(6), 1217–1237, DOI: 10.1007/s10825-024-02213-1.
68 H. Ledbetter and A. Migliori, *J. Appl. Phys.*, 2006, **100**, 063516.
69 V. Tvergaard and J. W. Hutchinson, *J. Am. Ceram. Soc.*, 1988, **71**, 157.
70 P. Lloveras, T. Castán, M. Porta, A. Planes and A. Saxena, *Phys. Rev. Lett.*, 2008, **100**, 165707.
71 M. H. Rubel, K. M. Hossain, S. K. Mitro, M. M. Rahaman, M. A. Hadi and A. Islam, Comprehensive First-Principles Calculations on Physical Properties of ScV2Ga4 and ZrV2Ga4 in Comparison with Superconducting HfV2Ga4, *Mater. Today Commun.*, 2020, 100935, DOI: 10.1016/j.mtcomm.2020.100935.
72 H. Ledbetter and A. Migliori, A General Elastic-Anisotropy Measure, *J. Appl. Phys.*, 2006, **100**, 063516, DOI: 10.1063/1.2338835.
73 V. Tvergaard and J. W. Hutchinson, *J. Am. Ceram. Soc.*, 1988, **71**, 157.
74 R. Majumder, S. K. Mitro and B. Bairagi, Influence of Metalloid Antimony on the Physical Properties of Palladium-Based Half-Heusler Compared to the Metallic Bismuth: A First-Principle Study, *J. Alloys Compd.*, 2020, 155395, DOI: 10.1016/j.jallcom.2020.155395.
75 Q. Li, S. Fang, X. Yang, Z. Yang, Q. Li, W. Zhou, D. Ren, X. Sun and J. Lu, Photodetector Based on Elemental Ferroelectric Black Phosphorus-like Bismuth, *ACS Appl. Mater. Interfaces*, 2024, **16**(46), 63786–63794, DOI: 10.1021/acsami.4c14392.
76 R. Gaillac, P. Pullumbi and F.-X. Coudert, *J. Phys.: Condens. Matter*, 2016, **28**, 275201.
77 R. K. Sharme, M. Muntasir, J. Patel, J. G. del Hoyo, L. R. de Marcos, M. A. Quijadab, and M. M. Rana, in *Image Sensing Technologies: Materials, Devices, Systems, and Applications XII*, SPIE, 2025, pp. 115–133.

78 O. L. Anderson, A Simplified Method for Calculating the Debye Temperature from Elastic Constants, *J. Phys. Chem. Solids*, 1963, 909–917, DOI: 10.1016/0022-3697(63)90067-2.
79 N. Jamila, I. J. Farah, J. K. Modak, W. Hasan, M. A. Rahman, M. M. Hossain, M. Rasheduzzaman, M. S. H. Choudhury, S. Chowdhury and R. Rahaman, DFT Based Computational Investigations of the Physical Properties of Perovskites-Structure SrXO3 (X= Si, Tb, Th) for Optoelectronic and Thermo-Mechanical Applications, *Mater. Today Commun.*, 2024, 107650, DOI: 10.1016/j.mtcomm.2023.107650.
80 T. Kraska, Molecular-dynamics simulation of argon nucleation from supersaturated vapor in the NVE ensemble, *J. Chem. Phys.*, 2006, **124**, 054507, DOI: 10.1063/1.2162882.